HHS Public Access

Author manuscript

Nat Neurosci. Author manuscript; available in PMC 2019 July 21.

Published in final edited form as:

Nat Neurosci. 2019 February ; 22(2): 229–242. doi:10.1038/s41593-018-0313-z.

Dysregulated protocadherin-pathway activity as an intrinsic defect in iPSC-derived cortical interneurons from patients with schizophrenia

Zhicheng Shao[1,14,17], **Haneul Noh**[1,2,17], **Woong Bin Kim**[3], **Peiyan Ni**[1,2], **Christine Nguyen**[1], **Sarah E. Cote**[1], **Elizabeth Noyes**[1], **Joyce Zhao**[1], **Teagan Parsons**[1], **James M. Park**[2], **Kelvin Zheng**[2], **Joshua J. Park**[2], **Joseph T. Coyle**[1], **Daniel R. Weinberger**[4], **Richard E. Straub**[4], **Karen F. Berman**[5], **Jose Apud**[5], **Dost Ongur**[1], **Bruce M. Cohen**[1], **Donna L. McPhie**[1], **Judith L. Rapoport**[6], **Roy H. Perlis**[7], **Thomas A. Lanz**[8], **Hualin Simon Xi**[9], **Changhong Yin**[10], **Weihua Huang**[10], **Teruyoshi Hirayama**[11,16], **Emi Fukuda**[11], **Takeshi Yagi**[11], **Sulagna Ghosh**[12], **Kevin C. Eggan**[12], **Hae-Young Kim**[13], **Leonard M. Eisenberg**[15], **Alexander A. Moghadam**[2], **Patric K. Stanton**[2], **Jun-Hyeong Cho**[3,18], and **Sangmi Chung**[1,2,18]

[1.]Department of Psychiatry, McLean Hospital/Harvard Medical School, Belmont, Massachusetts, USA

[2.]Department of Cell biology and Anatomy, New York Medical College, Valhalla, New York, USA

[3.]Department of Molecular, Cell and Systems Biology, University of California, Riverside, Riverside, California, USA

[4.]Lieber Institute for Brain Development, Johns Hopkins University, Baltimore, Maryland, USA

[5.]Clinical and Translational Neuroscience Branch, National Institute of Mental Health, National Institutes of Health, Intramural Research Program, Maryland, USA

[6.]Child Psychiatry Branch, National Institute of Mental Health, Bethesda, Maryland, USA

[18] Correspondence: schung8@nymc.edu, juncho@ucr.edu.

Authors contributions:

Z.S., H.N., P.N., W.-B.K., J.T.C., R.H.S., B.M.C., T.H., E.F., T.Y., S.G., K.C.E., A.A.M., P.K.S., J.-H.C., and S.C. designed the experiments.

Z.S., H.N., P.N., C.N., S.E.C., E.N., J.Z., T.P., J.M.P., K.Z. and J.J.P. performed analysis of iPSC-derived interneurons. W.-B.K., A.A.M., P.K.S. and J.-H.C. performed electrophysiological studies. T.A.L., H.S.X., C.Y. and W.H. did RNAseq analysis. T.H., E.F. and T.Y. generated PCDHA KO mice and performed behavioral analysis of PCDHA KO mice. R.E.S., S.G. and K.C.E. performed genotype analysis. L.M.E performed confocal analysis. H.-Y.K. performed statistical analysis.

H.N., J.T.C., T.A.L., H.S.X., W.H., T.H., E.F., T.Y., S.G., K.C.E., A.A.M., P.K.S., J.-H.C., and S.C. wrote the manuscript.

D.R.W., R.E.S., K.F.B., J.A., D.O., B.M.C., D.L.M., J.L.R. and R.H.P. provided patient cell lines and reviewed data interpretation and manuscript contents.

T.H., T.Y., J.-H.C., and S.C. supported this study financially.

Accession codes

The RNA-seq data were deposited at the GEO <https://www.ncbi.nlm.nih.gov/geo/> and the accession number is GSE118313 and GSE121376.

Conflict of interest

Thomas Lanz and Hualin Simon Xi were employees of Pfizer, Inc at the time this work was performed.

Data availability

The RNA-seq data were deposited at the GEO with the accession numbers GSE118313 and GSE121376. The data that support the findings of this study are available from the corresponding authors upon request.

[7]Center for Quantitative Health, Massachusetts General Hospital, Boston, Massachusetts, USA

[8]Internal Medicine Research Unit, Pfizer Inc., Cambridge, Massachusetts, USA

[9]Computational Sciences, Pfizer Inc., Cambridge, Massachusetts, USA

[10]Department of Pathology, New York Medical College, Valhalla, New York, USA

[11]KOKORO-Biology Group, Laboratories for Integrated Biology, Graduate School of Frontier Biosciences, Osaka University, Japan

[12]Department of Stem Cell and Regenerative Biology, Harvard Stem Cell Institute, Harvard University, Cambridge, Massachusetts, USA.

[13]Department of Public Health, New York Medical College, Valhalla, New York, USA.

[14]Fujian Provincial Key Laboratory of Neurodegenerative Disease and Aging Research, Institute of Neuroscience, Medical College, Xiamen University, Xiamen, Fujian, China

[15]New York Medical College/Westchester Medical Center Stem Cell Laboratory, Departments of Physiology and Medicine, New York Medical College, Valhalla, New York, USA

[16]Present address: Department of Anatomy and Developmental Neurobiology, Tokushima University Graduate School of Medical Science, Japan

[17]equal contributors

Abstract

We generated cortical interneurons (cINs) from iPSCs derived from14 healthy controls (HC cINs) and 14 patients with schizophrenia (SCZ cINs). Both HC cINs and SCZ cINs were authentic, fired spontaneously, received functional excitatory inputs from host neurons, and induced GABA-mediated inhibition in host neurons *in vivo*. However, SCZ cINs had dysregulated expression of protocadherin genes, which lie within documented SCZ loci. Mice lacking protocadherin α showed defective arborization and synaptic density of prefrontal cortex cINs and behavioral abnormalities. SCZ cINs similarly showed defects in synaptic density and arborization, which were reversed by inhibitors of Protein Kinase C, a downstream kinase in the protocadherin pathway. These findings reveal an intrinsic abnormality in SCZ cINs in the absence of any circuit-driven pathology. They also demonstrate the utility of homogenous and functional populations of a relevant neuronal subtype for probing pathogenesis mechanisms during development.

Keywords

Schizophrenia; induced pluripotent stem cells; interneurons; protocadherin

Introduction

Schizophrenia (SCZ) is a devastating disease affecting 1% of the adult population worldwide. It is a highly heritable [1] neurodevelopmental disorder [2], characterized by positive symptoms (e.g., hallucinations and delusions), negative symptoms (e.g., apathy, anhedonia) and cognitive symptoms (e.g., impairments of memory, executive functions and

attention) [3]. Cognitive and negative symptoms persist even with antipsychotic treatment [4], preventing normal functioning of patients. Given the fact that SCZ remains the seventh most costly medical disorder in our society, it is imperative to unravel its pathogenic mechanisms to develop novel and efficacious treatments.

So far, a large genome wide association study (GWAS) of SCZ has convincingly identified 108 risk loci with genome-wide significance [5], opening the way to a deeper understanding of SCZ pathogenic mechanisms. However, deciphering how these risk loci affect gene expression and result in SCZ pathogenesis is not a trivial task. Recent studies are making progress in this regard and have shown correlations between risk locus genotypes and gene expression levels (e.g. *FURIN* and *C4A*) [6,7]. However, whether the observed manner of gene expression changes cause SCZ-relevant neuro-anatomic and behavioral deficits in animal models needs to be determined. One caveat in current expression quantitative trait loci (eQTL) studies is that most of the attempts to connect gene expression levels with risk loci are based on transcriptome studies carried out on postmortem tissues [6], which typically involve subjects with chronic illness and years of exposure to psychotropic medications. Such studies cannot address pathogenic mechanisms operational during development [2]. Thus, disease-specific developmental brain tissue will be needed to unravel the role of these risk genes during the critical developmental periods. Induced pluripotent stem cell (iPSC) technology [8] allows us to generate such patient-specific developmental brain tissues with the same genetic make-up as the patient brains.

SCZ modeling using iPSCs has begun [9], and there has been a steady stream of studies reporting SCZ-specific transcriptome aberrations and cellular phenotypes in iPSC-derived neural tissues [10]. It will be important to sort out causal abnormalities vs. changes in effectors downstream of causal abnormalities. Correlation with genetic risk loci will provide a pathway for identifying causal abnormalities. In addition, animal model studies can help determine causal abnormalities that can recapitulate SCZ-like histological and behavioral abnormalities. One note of caution in using iPSC-derived neural tissues for studying SCZ pathology is the heterogeneity and stochasticity of iPSC-derived tissues, which can result in inconsistency due to the changing composition of neuronal subtypes within culture. Single cell RNA-seq can be used to address this problem. However, due to the more limited sequencing depth inherent to single cell RNA-seq, it is not as easy to identify differences in low abundance genes, which could play critical roles. Thus, generation of a homogeneous and consistent population of neural subtypes is critical for successful disease modeling using iPSCs.

Cortical GABAergic interneurons (cINs) are one of the most consistently affected neuronal types in SCZ, especially medial ganglionic eminence (MGE)-derived parvalbumin $(PV)^+$ or somatostatin $(SST)^+$ expressing cINs, as shown in numerous post-mortem studies [11,12]. In line with these findings, a role for altered GABA neurotransmission in SCZ was suggested to disrupt cortical gamma oscillations and thus cause cognitive deficits in patients [13]. Accordingly, $GABA_A$ receptor agonists were shown to restore gamma band activity in SCZ patients, accompanied by some degree of improved cognitive functions [14]. Furthermore, developmental cIN hypofunction resulted in a SCZ-like phenotype, including deficits in

dopaminergic systems in adult mice [15], suggesting a role of impaired cIN development in SCZ pathogenesis.

In this study, we used homogeneous populations of cINs derived from iPSCs to analyze cIN-intrinsic deficits in SCZ and found that the protocadherin pathway is significantly altered in SCZ cINs early in development. cINs in the prefrontal cortex (PFC) of *Pcdha* knockout (KO) mice showed arborization and synaptic deficits. In line with this, knock down (KD) of protocadherins in healthy control (HC) cINs resulted in significant reduction in arborization. Developmental SCZ cINs displayed arborization deficit in cell culture and synaptic deficits *in vivo* following transplantation into mouse brains. These deficits were also observed in cINs in SCZ postmortem PFCs. Inhibitors of protein kinase C (PKC), a downstream kinase in the protocadherin signaling pathway, normalized the arborization deficits observed in SCZ cINs. This study has revealed intrinsic deficits in SCZ cINs in the absence of any circuit-mediated deficits and demonstrates the utility of iPSC-derived homogeneous neural subtypes to illuminate the mechanistic basis of SCZ pathogenesis and to identify potential novel therapeutic targets.

Results

Homogeneous populations of cINs were generated from HC and SCZ iPSCs

As the first step to study the SCZ pathogenic mechanisms in disease-relevant developmental tissues, we generated iPSCs from HC and SCZ fibroblasts using footprint-free modified RNA methods [16]. Footprint-free reprogramming is even more important for studying SCZ where multiple single nucleotide polymorphisms (SNPs) with small effects work together to result in pathogenesis. We chose Caucasian male patients to reduce variation caused by ethnicity and gender. Further, we chose patients who required clozapine treatment to narrow down the patient group to those with more severe cases of the disease (Figure 1a). iPSCs reprogrammed with modified RNA transfection [16] showed human pluripotent stem cell (hPSC)-like morphology and expressed hPSC markers (Figure 1b).

To obtain a homogeneous population of developmental cINs from generated iPSCs, we differentiated them using the protocol we optimized previously [17] with a slight modification (Figure 1c). This protocol generated a homogeneous population of developmental cINs from multiple iPSC lines. The homogeneity was extensively analyzed by expression of the neuronal marker, β-tubulin III, MGE-derived cIN marker SOX6 [18], and GABA-synthesizing enzyme glutamate decarboxylase 1 (GAD1) (Figure 1d-e and Supplementary Fig. 1). CGE-derived cINs or non-cIN neural subtypes were only rarely observed regardless of their disease status (Supplementary Fig. 2). We further analyzed the phenotypes of the generated cINs by quantitative real time polymerase chain reaction (PCR) analysis, comparing them with undifferentiated iPSCs and induced glutamatergic neurons [19]. We observed that cIN-specific genes (*GAD1, LHX6, NKX2–1 and SOX6*) are highly expressed in cIN groups but not in the other cell groups. On the other hand, there was minimal expression of non-cIN markers (*NANOG, PAX6, TBR1 and SLC17A7 (Vglut1)*) in generated cINs (Figure 1f), confirming the identity and homogeneity of the generated cells. The homogeneity of differentiated progeny is critical for the reliable transcriptome analysis of developing cINs.

Neuronal and synaptic properties of cINs transplanted into mouse cerebral cortex

Previous studies on cIN induction from human PSCs focused on human embryonic stem cell-derived cINs, and thus it was unclear whether cINs derived from iPSCs, which went through the reprogramming process from skin cells, are authentic and functional, and thus suitable for disease modeling. To address this, we performed extensive electrophysiological analysis after grafting these cells into mouse brains. HC and SCZ cINs were transduced with lentivirus expressing channelrhodopsin 2 (ChR2) (H134R)-green fluorescence protein (GFP) fusion protein under the control of the synapsin promoter (LV-Syn-ChR2 (H134R)-GFP) to permit optogenetic study as well as the identification of grafted cells in brain slices. They were then transplanted into the cerebral cortices of Nod Scid mice, followed by electrophysiological analysis 7 months after transplantation (Figure 2a). In GFP^+ grafted cells, blue light illumination induced typical ChR2-mediated currents (Figure 2b) and evoked action potential (AP) firings (Supplementary Fig. 3a). The passive membrane properties of SCZ cINs, including membrane resistance (R_m) and membrane capacitance (C_m), were similar to those in the HC group (Supplementary Fig. 3b–c). When depolarizing voltage pulses were applied, grafted cINs showed rapidly desensitizing inward currents and sustained outward currents (Figure 2c), indicating the expression of voltage-gated Na^+ channels and K^+ channels. There was no difference between groups in the voltage-dependent Na^+ current density (Supplementary Fig. 3d) and the K^+ current density (Supplementary Fig. 3e).

In current-clamp mode, the injection of depolarizing currents induced AP firings in all human cINs examined (Figure 2d). Non-accommodating repetitive AP firings were observed in >75% of the grafted cINs in both groups, whereas grafted cells in the remaining proportion displayed single or burst AP firing patterns. The frequency of AP firings induced by current injection was comparable between groups (Figure 2e) with no significant difference in afterhyperpolarization (AHP), AP threshold and AP half-width (Supplementary Fig. 3f–h). However, the resting membrane potential (RMP) of the cINs was significantly more depolarized in the SCZ group than in the HC group (Supplementary Fig. 3i). At RMP, spontaneous AP (sAP) firings were observed in >80% of human cINs in both groups (Figure 2f and Supplementary Fig. 3j), with comparable sAP frequency between groups (Supplementary Fig. 3k), suggesting that most grafted cINs generate tonic spontaneous firings in both the SCZ and HC groups. Neuronal properties of iPSC-derived cINs were also confirmed *in vitro* (Supplementary Fig. 4). These results demonstrate that HC and SCZ cINs develop into functional cINs whose neuronal properties are similar to those of endogenous interneurons.

We next analyzed the synaptic properties of grafted human cINs to determine whether they integrate into adult brain circuitry and receive excitatory synaptic inputs from host cortical neurons. In acute cortical slices, all 26 GFP^+ grafted interneurons showed spontaneous excitatory postsynaptic currents (sEPSCs) at –85 mV in voltage-clamp mode (Figure 2g). These currents were inhibited completely by NBQX, a glutamate receptor antagonist, in all 3 grafted cells examined, indicating that they were mediated by the excitatory neurotransmitter, glutamate. There was no significant difference in the frequency or amplitude of sEPSCs between the HC and SCZ groups (Supplementary Fig. 5a–c). These

results suggest that human cINs from both HC and SCZ groups have functional postsynaptic machinery to receive excitatory synaptic inputs from host glutamatergic cortical neurons.

We also examined whether grafted human cINs had presynaptic mechanisms for the release of GABA, which induces inhibitory postsynaptic responses in host cortical neurons. To this end, we used optogenetic approaches to selectively stimulate grafted cINs expressing ChR2-GFP and record postsynaptic responses in GFP^{-} host cortical neurons (Figure 2h-i). Short pulses of blue light illumination induced postsynaptic currents at 0 mV in voltage-clamp mode, which were inhibited completely by SR95531, a $GABA_A$ receptor antagonist (Figure 2j), indicating that they were mediated by inhibitory neurotransmitter GABA. Proportions of host neurons with IPSCs were comparable between groups (Figure 2k-l), suggesting the majority of recorded host neurons received inhibitory inputs from grafted cINs. Moreover, the peak amplitude of inhibitory postsynaptic currents (IPSCs) induced by photostimulation was not significantly different between groups (Figure 2k-l and Supplementary Fig. 5d). Our power analysis indicates that we would need to record from 196 host neurons to achieve 80% power for detecting a 36.5 pA mean difference with standard deviation = 57.2 pA and intra-cluster correlation = 0.2, pointing to the large sample size needed to detect mild phenotypes of SCZ. These results demonstrate that grafted cINs have presynaptic machinery for GABA release and inhibit host cortical neurons.

PCDHA2 expression is altered in SCZ cINs

Given the evidence that iPSC-derived HC and SCZ cINs are authentic and fully functional interneurons, we then asked whether there were any SCZ cIN-specific abnormalities in gene expression during development. We performed RNA-seq analysis, comparing transcriptomes of HC cINs to SCZ cINs after 8 weeks' differentiation. A total of 273 million reads were obtained from 8 lines (4 HC and 4 SCZ) with three independent differentiations (Supplementary Fig. 6a). The total number of genes were similar among different RNA-seq reactions (Supplementary Fig. 6b), suggesting that the read depth from each RNA-seq was sufficient to identify most of the genes expressed. When we performed a pair-wise comparison, the average r^2 value for biological replicates was about 0.95, showing high correlation that reflects the homogeneous and efficient cIN generation from iPSCs (Supplementary Fig. 6c). Along the same line, the average r^2 between individuals in this study was about 0.93, as compared to about 0.82 for postmortem tissues (Supplementary Fig. 6c), stressing the consistency of iPSC-derived cIN samples. Principal component analysis showed that biological replicates from the same individual tend to cluster together (Supplementary Fig. 6d), whereas there is no clear separation based on diagnostic group, indicating the subtle nature of SCZ phenotype (Supplementary Fig. 6d–e). Neuronal markers (MAP2 and DCX) and cIN markers (GAD1, VGAT, SST and Lhx6) were highly expressed, whereas the expression of non-relevant markers such as GFAP (astrocyte marker), MBP (oligodendrocyte marker), Vglut2 (glutamatergic neuron marker), CoupTFII (CGE-derived cIN marker), Olig2 (early MGE progenitor marker), ChAT (cholinergic neuron marker), TH (dopaminergic neuron marker) and TPH2 (serotonergic neuron marker) were low (Figure 3a and Supplementary Fig. 7a). Notably, expression of those markers did not differ between HC and SCZ (Figure 3a). While the global gene expression pattern did not show clear separation between HC and SCZ, select genes did exhibit significant differences in expression between

SCZ and HC, such as *PCDHA2* (Figure 3b and Supplementary Fig. 6f), which was confirmed by real time PCR analysis (Figure 3c).

To test whether alteration in *PCDHA2* expression is also observed in other neuronal subtypes, we generated glutamatergic neurons using the Ngn2 induction protocol [19] with a slight modification (Figure 3d). Glutamatergic neurons could be efficiently generated from both HC and SCZ iPSCs (Figure 3e). Real time PCR analysis showed no significant change in *PCDHA2* expression in SCZ glutamatergic neurons (Figure 3f). Further studies will reveal whether this observation is universal for all developmental glutamatergic neurons rather than just induced glutamatergic neurons analyzed here.

Downregulation of multiple protocadherin family members in SCZ cINs

Considering the heterogeneity of SCZ etiology, we expanded the sample size and performed RNA-seq analysis on a larger cohort with 14 HC lines and 14 SCZ lines after 8 weeks' differentiation (Figure 4a). Again, the same patient selection criteria was employed with Caucasian Males who required Clozapine treatment. In addition to *PCDHA2*, there are additional *PCDHA* genes that are down regulated in SCZ cINs, including *PCDHA3, 6* and *8* (Figure 4b). Real time PCR analysis confirmed significant decreases of these PCDHA family members in SCZ cINs (Figure 4c), whereas expression of *PCDHA3, 6* and *8*, like *PCDHA2*, was not altered in SCZ glutamatergic neurons (Supplementary Fig. 8a).

Publicly available eQTL databases (https://www.gtexportal.org, https://www.synpase.org/cmc) showed that there are numerous *PCDHA2* eQTL SNPs with high SCZ association (Supplementary Fig. 8b), suggesting a potential role of SCZ risk loci in regulating expression of *PCDHA2*. We selected rs7445192 for genotype-gene expression correlation analysis due to its high correlation with SCZ with a higher odd ratio and significant eQTL status for *PCDHA2* (Supplementary Fig. 8c). There was a trend of decreasing *PCDHA2* expression in iPSC-derived cINs with more alternate alleles (A) of rs7445192 (Figure 4d), though this did not reach statistical significance. Power analysis showed that 256 samples would be needed to reach statistical significance. Searches in the CommonMind portal showed that *PCDHA2* has 533 eQTL SNPs and *PCDHA3* has 0 eQTL SNPs. *PCDHA6* has 88 eQTL SNPs, but rs7445192 was not one of them (Supplementary Fig. 8d). Interestingly, we did not see genotype-expression level correlation in these two genes without a previous eQTL connection with this SNP (Figure 4d). *PCDHA8* has 800 eQTL SNPs, including rs7445192, and also shows the tendency of decreasing expression by more alternate alleles (Figure 4d), though again this finding did not reach statistical significance. Power analysis showed that 226 samples would be needed to reach statistical significance.

In addition to *PCDHA* members, the majority of other protocadherin members were also downregulated in SCZ cINs (Figure 4e). Real time PCR analysis confirmed significant decreases of all *PCDHA* and *PCDHG* family members in SCZ cINs, using primers against the *PCDHA*-constant region (CR) and *PCDHG*-CR (Supplementary Fig. 8e). However, expression of these genes was not altered in SCZ glutamatergic neurons (Supplementary Fig. 8f). The publicly available eQTL databases showed that other highly affected protocadherins also had eQTL within the SCZ risk loci (Chr5:140,023,664–140,222,664) a little bit further from the area where most of their eQTL reside (Figure 4f and

Supplementary Fig. 8g). This suggests that this SCZ risk locus may be related to the regulation of multiple protocadherin family members in addition to *PCDHA* members.

Altered PFC cIN development and impaired prepulse inhibition in *Pcdha* KO mice

Having observed downregulation of multiple protocadherin family members, including *PCGHA* and *PCDHG*, in SCZ cINs, we examined the effect of protocadherin hypofunction on cIN development using a mouse model with a *Pcdha* null mutation (Δα/Δα) [20], where all members of the *Pcdha* family are knocked out. *Pcdhg* is necessary for proper *Pcdha* localization and function [20,21] (but not the other way around). As such, *Pcdhg* KO mice show severe lethal phenotypes, unlike *Pcdha* KO mice, which show mild phenotypes. Thus, we used the partially compromised protocadherin function in *Pcdha* KO mice to model the protocadherin hypofunction seen in SCZ cINs. We analyzed the arborization of PFC cINs within 150 μm from the cell bodies and found a mild but significant arborization deficit in *Pcdha* KO cINs, shown by significant decreases in neurite number from soma, total branch number, and total neurite length (Figure 5a and Supplementary Fig. 9a). We also observed deficits in inhibitory synapse formation of PFC cINs in *Pcdha* KO mice by analyzing the number of $VGAT^+$ puncta on PV^+ cINs that were juxtaposed to $Gephyrin^+$ puncta (Figure 5b and Supplementary Fig. 9b). However, there was no significant difference in the excitatory synapses that cINs receive between *Pcdha* KO mice and littermate wild type controls (Figure 5c and Supplementary Fig. 9c). These results suggest the importance of the protocadherin pathways in the normal development of cINs in the PFC.

Previous studies have shown that *Pcdha* KO mice harbor projection and connection deficits in different brain regions and display deficits in contextual learning and working memory [21], which are relevant to the SCZ clinical phenotype. We tested whether *Pcdha* KO mice show deficits in prepulse inhibition (PPI), which occur in many SCZ patients and can be attenuated by antipsychotic treatment [22]. *Pcdha* CR KO mice [23], which have non-functional *Pcdha* expression, showed significant deficits in PPI compared to their wild type littermates (Figure 5d). In addition, *Pcdha* hypomorphic mice (ΔBneo/ΔBneo) [24] also showed significant PPI deficits (Figure 5e), suggesting the importance of the protocadherin pathway for normal sensorimotor gating.

Deficits in arborization and synaptic density in SCZ cINs

Having observed cIN deficits by protocadherin hypofunction during cIN development, we tested whether SCZ cINs also demonstrate similar phenotypic deficits. To analyze arborization, we infected HC and SCZ cINs with a limiting titer of lentivirus expressing GFP under the Ubiquitin promoter (LV-Ubi-GFP) to label cells only scarcely. We then traced and analyzed GFP^+ cells. There was a mild but significant decrease in neurite number from the soma, total branch numbers, and total neurite lengths in SCZ cINs compared to HC cINs (Figure 6a). Linear regression analysis showed that the expression level of *PCDHA2, PCDHA3, PCDHA6* and *PCDHA8* has weak or mild correlation with arborization (Supplementary Fig. 10a). It was shown that in the excitatory glutamatergic neuronal context, protocadherin CR inhibits focal adhesion kinase (FAK) and in turn, PKC [25], which otherwise inhibits arborization by inactivating MARCKS via phosphorylation [21,25]. Thus, we tested whether treating SCZ cINs with PKC inhibitors can reverse this deficit by

protocadherin hypofunction. Treatment with the PKC inhibitor GO6893 reversed the arborization deficit in the SCZ cINs, whereas it did not produce a significant difference in HC cINs (Figure 6b and Supplementary Fig. 10b). To more directly test the effect of lower protocadherin expression on cINs, we performed gene KD experiments against the *PCDHA*-CR or the *PCDHG*-CR that knock down entire *PCDHA* or *PCDHG* families (Supplementary Fig. 10c). One-month old cINs were transfected with negative control siRNA, *PCDHA* siRNA, *PCDHG* siRNA or *PCDHA* siRNA+*PCDHG* siRNA, infected with limiting titer of LV-Ubi-GFP virus, and traced at 7 days after transfection. There was a mild but significant decrease in arborization of HC cINs by *PCDHA* KD or *PCDHG* KD and to a lesser degree in SCZ cINs (Figure 6c and Supplementary Fig. 10d).

To study HC and SCZ cINs in an *in vivo* circuit environment, we transplanted 8 weeks-old cINs to the cerebral cortices of Nod Scid mice after labeling them with LV-Syn-ChR2 (H134R)-GFP and analyzed their phenotypes (Figure 7a). One of the characteristic behaviors of developing cINs is robust migration even in transplanted adult brains, comparable to their extensive migration during early development [26]. iDISCO$^+$ clearing [27] and Light sheet microscopy showed robust migration of grafted cINs (Figure 7b), up to 2,000 μm from the injection site in the adult mouse cortex (Figure 7c-d). We further characterized cINs in the brain environment by immunocytochemistry. Consistent with their MGE-derived phenotype, many grafted cINs express either MEF2C, a marker enriched in PV$^+$ interneuron precursors in mice [28], or SST (Figure 7e), regardless of their disease status. We also observed that small proportion of cINs started to express PV, regardless of their disease status (Supplementary. Fig. 11a). Overall these results suggest that there was no difference in cIN fate determination between HC and SCZ populations. Synapse analysis showed a mild but significant deficit in inhibitory synapse formation by SCZ cINs compared to HC cINs (Figure 7f and Supplementary Fig. 11b). The excitatory synapse density did not differ between grafted HC cINs and SCZ cINs (Figure 7g and Supplementary Fig. 11c). Linear regression analysis showed that expression level of *PCDHA2, PCDHA3, PCDHA6* and *PCDHA8* has weak or mild correlation with inhibitory synapse formation (Supplementary Fig. 11d). These results suggest that SCZ cINs have an intrinsic deficit in the formation of inhibitory synapses in the absence of a SCZ circuit environment.

Synaptic and arborization deficits in cINs in postmortem brains from SCZ patients

Having observed developmental SCZ cIN-intrinsic phenotypic deficits, we sought to explore whether the observed developmental deficits continue to be present in adult post mortem brains. Thus, we analyzed layer 3 PV$^+$ cINs from 8 HC vs. 8 SCZ postmortem PFCs (Figure 8a). Arborization analysis showed a mild but significant deficit in SCZ postmortem cINs, shown by significant decreases in neurite number from soma, total branch number, and total neurite length (Figure 8b and Supplementary Fig. 12a). This was consistent with the phenotypes observed in developmental cINs. A mild but significant deficit in inhibitory synapse formation was observed also in postmortem SCZ cINs in the PFC (Figure 8c and Supplementary Fig. 12b), again consistent with results from developmental cINs. However, unlike in the developmental SCZ cINs, excitatory synapse formation was significantly reduced in postmortem SCZ cINs (Figure 8d and Supplementary Fig. 12c), possibly due to deficits in glutamatergic neurons.

Discussion

In this study, we have found that the expression of protocadherins, genes within well-documented SCZ risk loci [5], are significantly downregulated in SCZ cINs during development and that their altered expression resulted in disease-relevant phenotypes in KO mice and human SCZ cINs. The discovery of altered expression of genes within SCZ risk loci is important as it may shed light on the causal pathophysiology of SCZ. The presence of numerous significant eQTL SNPs for *PCDHA* members within SCZ risk loci suggests that this particular SCZ risk locus may regulate *PCDHA* gene expression. The modest change of *PCDHA* gene expression we observed is in agreement with the previous large scale eQTL studies for SCZ risk loci [6]. Also, it is consistent with the notion that small changes in many genes may epistatically cause the disease phenotype, stressing the importance of studying "pathway" changes instead of "single gene" changes to better understand SCZ pathogenesis. Interestingly, the direction of expression alterations by risk alleles are different depending on the brain regions examined, stressing the importance of using disease-relevant and homogeneous cell populations to understand the effect of the risk genotype.

Protocadherins are a family of cell surface proteins that play important roles during brain development [21]. They are transferred between the cell surface and intracellular organelles [29,30] and cell surface localization of PCDHA was shown to be facilitated by forming a heterodimer with PCDHG [31,32]. Once on the cell surface, PCDHA, often times as a heterodimer with PCDHG, inhibits the FAK-PKC pathway that inhibits neurite arborization, thereby facilitating neuronal arborization [25,33]. PCDHA is robustly expressed during late embryonic to early postnatal period in axons, then, expression deceases with myelination [34,35], suggesting its role in axonal path finding and arborization. In this study, we observed that *Pcdha* deficiency results in an arborization defect in cINs in *Pcdha* KO mouse PFC as well as in SCZ cINs *in vitro*, which was reversed by inhibiting PKC, downstream in the protocadherin pathway. In addition to their role in arborization, PCDHA and PCDHG proteins are localized to synapses during development [29,30,36], but not in many mature neurons [21], suggesting their role during synaptogenesis. Consistent with this inference, we observed an inhibitory presynaptic deficit in cINs both in the *Pcdha* null mice PFC as well as in SCZ cINs transplanted into mouse cortex. Downregulation only in *PCDHA* members is not likely to generate protocadherin-related phenotypes in SCZ cINs, considering the mild phenotype observed in *Pcdha* KO mice, unlike the severe lethal phenotypes of *Pcdhg* KO mice [37]. However, down-regulation of many members of the protocadherin family, including both *PCDHA* and *PCDHG*, may explain the observed mild phenotype in SCZ cINs. Modest abnormal phenotype in SCZ cINs is in line with the overall mild pathology of SCZ observed in postmortem studies.

SCZ is a uniquely human disease, not easy to model behaviorally in animals, but there are animal models where environmental and genetic risk factors generate SCZ-like behaviors [38]. SCZ patients display sensory motor gating deficits, cognitive deficits and anhedonia, and these deficits can be seen in animal models of SCZ. Previously, it was reported that *Pcdha* null mutant mice have a working memory deficits [21,24]. In addition, in this study, we observed *Pcdha* null mutant mice and *Pcdha* hypomorphic mice display deficits in PPI, indicating that reduced *Pcdha* expression results in impaired sensory motor gating. This

behavioral deficit is consistent with SCZ-like histological deficits that we observed in PFC cINs in *Pcdha* null mice and suggests the role of reduced PCDHA expression in SCZ pathogenesis.

Previously, it was not clear whether cIN hypofunction in SCZ PFC was due to intrinsic defects in cINs and/or as a result of hypofunction of glutamatergic input into cINs. In this study, using homogeneous population of cINs without presence of any SCZ glutamatergic input, we could observe cIN-intrinsic abnormalities *in vitro and in vivo*. These findings demonstrate the potential of homogeneous iPSC-derived neural subtypes for unraveling disease mechanisms. In this example, the mixed cell populations used in most previous iPSC disease modeling studies [10] would not have allowed detection of cell type-specific pathological changes of minor populations. We also obtained a homogeneous population of glutamatergic neurons using Ngn2-based induction, a well-accepted protocol in the field [39], though there is a caveat that the induced glutamatergic neurons may not be identical to *in vivo* glutamatergic neurons. In addition to the homogeneity and consistency of generated cINs, the opportunity to perform extensive electrophysiological characterization gave us confidence about their authenticity and functionality. In this study, IPSCs in host cortical neurons induced by stimulation of grafted cINs were not significantly different between groups, although significant differences were detected in synapse analysis. This could be due to small sample size of our electrophysiological experiments and/or compensatory mechanisms [40] in human cINs transplanted into normal mice brains. In the future, further technical developments that allow high throughput analysis, such as the Patch Clamp array, will be pivotal to obtaining enough power to electrophysiologically study mild SCZ phenotypes. iPSC-derived human disease tissues provide a method to screen chemicals to correct identified cellular phenotypes, thus providing unprecedented opportunities to develop mechanistic treatments. This is especially important, considering the fact that the complex genetics of SCZ, with over a hundred risk alleles already identified, each having only a modest effect, are difficult to replicate in experimental animals. Not surprisingly, many effective treatments developed in animal models have failed in human clinical trials [41,42]. In our study, we have observed that treatment with a PKC inhibitor corrects the abnormal cellular phenotype in SCZ cINs. In this regard, it is interesting to note that a PKC inhibitor was successfully used to treat acute mania in bipolar disorders in small scale clinical trials [43–45], as bipolar disorder shows substantial clinical and genetic overlap with SCZ [46].

Reduction in synapse density in both excitatory synapses and inhibitory synapses have been reported in SCZ postmortem studies [47,48], and the decrease in the number of inhibitory synapses in developmental SCZ cINs is in line with that observation. However, we do not see fewer excitatory synapses in developmental cINs transplanted into the mouse cortex but only in postmortem cINs. This can be explained if the decrease seen in human postmortem brains is due to the reduction in excitatory output from glutamatergic neurons rather than the intrinsic deficit of interneurons in receiving excitatory input. In addition, whereas numerous postmortem studies confirmed reduced GAD expression in SCZ interneurons, we did not see such defects in these developmental cIN populations. This discrepancy could be a consequence of comparing cells in culture with cells *in vivo*, or may have resulted from differences in interneuron age or subtypes. Also, it could be due to the fact that GAD expression is regulated in an activity-dependent manner [49]. Thus, rather than being an

intrinsic deficit of SCZ interneurons, the reduction in GAD expression could have appeared only in the circuit environment with defective SCZ glutamatergic neurons.

In summary, the discovery of disrupted gene expression within SCZ risk loci, along with the animal and cell model effects, suggests the possibility of a causal relationship between protocadherins and SCZ. In addition, our study demonstrates the power of homogenous and functional populations of a specific neuronal subtype known to be affected in SCZ for probing the pathogenesis of schizophrenia, which may provide a pathway to identify more effective therapies and preventive interventions.

Methods

Generation of induced pluripotent stem cells

These study protocols were approved by the McLean Hospital/Partners Healthcare Institutional Review Board and New York Medical College Institutional Review Board. All procedures were performed in accordance with the Institutional Review Board's guidelines and all human samples were obtained with informed consents. We have complied with all relevant ethical regulations. Human fibroblasts were obtained from the laboratories of Dr. Bruce Cohen (McLean Hospital), Dr. Daniel Weinberger (Lieber Institute for Brain Development), and Dr. Judith Rapoport (National Institute of Mental Health). Skin biopsies were performed on HC and SCZ patients. The skin tissue was cut out under local anesthesia (2% lidocaine with or without epinephrine), washed with phosphate buffered saline (PBS) 3 times and placed in 35mm culture dishes. One drop of DMEM with Glutamax with 10% fetal bovine serum (FBS), 2% L-Glutamine, 1% Penicillin/Streptomycin solution (PS), and 1% Amphotericin and Gentamicin solution was added on each piece of skin and put in the incubator (37°C/5% CO_2). The skin samples in the culture dishes were changed with fresh media every other day to induce fibroblast cell growth as described in [50].

Human fibroblasts were reprogrammed using modified RNA methods [16] by Cellular Reprogramming, Inc. (San Diego, CA). Each fibroblast line was plated to 6-well plates without feeders at three different plating densities and subjected to messenger RNA reprogramming. Nascent colonies were bulk-passaged from the most productive well to establish passage 1 (P1) iPSC cultures on rLaminin-521 (BioLamina, Sweden) in Nutristem XF media (Biological Industries, Israel) and expanded in the same culture system until at least passage 3 before being characterized by 4'−6-diamidino-2-phenylindole (DAPI)/ OCT4/TRA-1–60 immunostaining and frozen down for storage.

Differentiation of iPSCs into cINs

Thawed human iPSCs were maintained on Matrigel (BD, San Hose, CA) coated plates with Essential 8 (E8) media (Invitrogen, Carlsbad, CA). For differentiation, iPSCs were trypsinized and grown as floating spheres in low adherent flasks in KSR media (DMEM, 15 % knockout serum replacement, 2 mM L-glutamine and 10 μM β-mercaptoethanol (all from Invitrogen)) from day 0 to day 14. For neuroectoderm induction, cells were treated with LDN193189 (100 nM, Stemgent, Cambridge, MA) from day 0 to day 14 and SB431542 (10 μM, Tocris Cookson, Ellisville, MO) from day 0 to day 7. For MGE

phenotype induction, media was supplemented with IWP2 (5 μM, EMD Millipore, Billerica, MA) from day 0 to day 7 and SAG (0.1 μM, EMD Millipore) from d0 to d21. From day 14, cells were grown in N2AA media (DMEM-F12 with N2-supplement (1:200, Invitrogen) and 200 μM ascorbic acid (AA, Sigma, St. Louis, MO)). FGF8 (100 ng/ml, Peprotech, Rocky Hill, NJ) was added from day 14 to day 21 to induce MGE phenotype at the expense of the CGE phenotype [17]. N2AA media was supplemented with 10 ng/ml glial cell derived neurotrophic factor (GDNF, Peprotech) and 10 ng/ml brain derived neurotrophic factor (BDNF, Peprotech) from day 21. At day 45 of differentiation, cIN spheres were trypsinized in the presence of 0.1M trehalose (Sigma) and then plated on polyornithine (PLO; 15 mg/ml; Sigma)- and fibronectin (FN; 1 mg/ml; Sigma)-coated plates in B27GB media (DMEM-F12 media with B27 supplement (1:100, Invitrogen), 10 ng/ml GDNF and 10 ng/ml BDNF). Cell lines differentiated for each experiment are summarized in Supplementary Table 3.

siRNA transfection

At day 28 of differentiation, cIN spheres were trypsinized and then plated onto PLO/fibronectin-coated plates in B27GB media. Two days after plating, cINs were transfected with negative control siRNA (Ribobio), PCDHA siRNA (siG180312020039, Ribobio), PCDHG siRNA (siB180425114250, Ribobio) and PCDHA/PCDHG siRNA (Ribobio) at a final concentration of 25 nM by using Lipofectamine® RNAiMAX Reagent (Life Technologies) according to the manufacturer's protocol. 6–8 hours after siRNA transfection, the cells were infected with a LV-Ubic-GFP virus, followed by arborization analysis 7 days after transfection.

Differentiation of iPSCs into Glutamatergic neurons

Human iPSC cells were seeded at a density of 10^6 cells/well on Matrigel-coated 6-well plates with E8 media, 5 μM Rock inhibitor Y-27632 (Selleck Chemicals, Houston, TX), Lentivirus that inducibly express Ngn2 and constitutively express Puromycin resistance gene (packaged using pLV_TRET_hNgn2_UBC_Puro plasmid from Addgene, Plasmid #61474 (Addgene, Cambridge, MA)), 2 μg/ml of Doxycycline and 2 μg/ml of polybrene. After overnight incubation (day 1), the media was replaced with N2AAGB media (DMEMF12 with N2 supplement (1:200), 200 μM ascorbic acid, 10 ng/ml GDNF and10 ng/ml BDNF) with 2 μg/ml of Doxycycline. At day 2, 1 μg/ml of Puromycin was added to the culture. At day 3, the media was changed with B27AAGB media (DMEMF12 with B27 Supplement (1:100), 200 μM ascorbic acid, 10 ng/ml GDNF and 10 ng/ml BDNF) and 2 μg/ml of Doxycycline and changed every other day until day 10. On days 11–14, the media was changed with B27AAGB media without doxycycline until the neurons were harvested for RNA preparation or fixed for immunocytochemistry on day 14 of differentiation.

Immunocytochemistry, Cell counting and Arborization analysis

Cells were fixed in 4% paraformaldehyde (PFA) for 10 min. The fixed cells were blocked in PBS with 10% normal serum and 0.1% Triton X-100 for 10 min at room temperature (RT). Cells were incubated with the primary antibody in PBS with 2% normal serum overnight at 4°C. After washing in PBS, the cells were incubated with the fluorescently-labeled secondary antibody in PBS with 2% normal serum for 1 hr at RT. Cell nuclei were also counterstained with DAPI (Invitrogen, 1:10,000). The antibodies used are GAD1 (AB1511,

Millipore), Glutamate (G-6642, Sigma Aldrich), PV (PV 25, Swant and PA5–47693, ThermoFisher), PSD95 (3450P, Cell Signaling), Vglut1 (73–066, UC Davis), VGAT (131 003, Synaptic Systems), Gephyrin (147 011, Synaptic Systems), SOX6 (AB5805, Millipore), b-Tubulin III (802001, Covance), OCT4 (CA0A3, Cell Signaling), Tra-160 (ab16288, Abcam), GFP (ab13970, Abcam), NCAM (sc-106, Santa Cruz Biotech), MEF2C (5030S, Cell Signaling), SST (sc-7819, Santa Cruz Biotech), Human Cytoplasm (AB-121-U-050, Stem Cells Inc.), VIP (20077, Immunostar), CCK (C2581, Sigma Aldrich), Calretinin (CG1, Swant), COUPTHII (PP-H7147–00, Perseus Proteomics), OLIG2 (AB9610, Millipore), ChAT (AB114P, Chemicon), TH (P40101–150, Pel-Freez) and 5-HT (20080, Immunostar) and summarized in Supplementary Table 1. More information on antibody validation can be found in the Life Sciences Reporting Summary. After washing in PBS, coverslips were mounted onto slide glasses using Fluoromount-G (Southern Biotech, Birmingham, AL). Fluorescent images were taken using the EVOS FL Auto microscope (Life Technologies, Carlsbad, CA) or Olympus DSU Spinning Disc Confocal on an IX81 inverted microscope (Olympus, Center Valley, PA).

For cell counting, Image J software (Version 1.51p, NIH, Bethesda, MD) was used to count the cell number using the multi point function. The experimenters were blind to the sample ID during data collection. Percentages of cells positive for each marker were quantified in relation to DAPI-stained nuclei from three independent differentiations, with a total of at least 500 cells counted for each line.

For arborization analysis, cells were infected with limiting concentration of LV-UbiC-GFP virus (MOI=0.001) to induce rare infections and fixed 10 days after infection for analysis. To test the effect of PKC inhibitor on arborization, cell cultures were treated with 5 μM of GO6893 or DMSO as a vehicle for 12 days before fixation. GFP^+ cells were traced using ImageJ software version 1.51 (NIH) with the NeuronJ plug in to obtain parameters of arborization such as neurite length, neurite number from soma, and branch number. The experimenters were blind to the sample ID during data collection.

RNA preparation and Real time PCR

RNA samples were isolated using a TRIzol-reagent (Invitrogen) and 300ng of the total RNA was used for cDNA synthesis using the $Oligo(dT)_{12–18}$ primer (Gene Link, Hawthorne, NY), Recombinant RNAse Inhibitor (Takara, Japan), 0.5 mM dNTP mix (Thermo Scientific, Waltham, MA), 5 mM DTT (Invitrogen), RevertAid H minus RT (Thermo Scientific), and 5X Reaction Buffer (Thermo Scientific) in SimpliAmp™ Thermal Cycler (Applied Biosystems, Waltham, MA). The primer sequences used for real time PCR are summarized in Supplementary Table 2. The real time PCRs were performed using the CFX Connect™ Real-Time PCR Detection System (BioRad, Hercules, CA), with 40 cycles of denaturation (95°C for 15sec), annealing (55°C for 30sec), and extension (72°C for 30sec).

Whole-cell patch-clamp recordings in brain slices

For electrophysiological studies, human cINs derived from human iPSCs were infected with LV-Syn-ChR2 (H134R)-GFP and were transplanted as described below. Seven months after transplantation, acute brain slices containing the cerebral cortex were prepared using a

vibrating microtome (Leica Biosystems, Germany) for electrophysiological analysis. After recovery, brain slices were placed in the recording chamber and continuously perfused at the rate of 1 mL per minute with artificial cerebrospinal fluid containing 130 mM NaCl, 2.5 mM KCl, 2.5 mM $CaCl_2$, 1 mM $MgSO_4$, 1.25 mM NaH_2PO_4, 26 mM $NaHCO_3$, and 10 mM glucose with 95 % O_2 and 5 % CO_2. Whole-cell patch-clamp recordings were performed at 30–32°C using a Multiclamp 700B amplifier, a Digidata 1550A or 1320A digitizer and Clampex 10 software (Molecular Devices, Sunnyvale, CA). For recording grafted interneurons (GFP^+ cells), the patch electrodes (~5 MOhm resistance) were filled with solution containing 150 mM K-gluconate, 5 mM NaCl, 1 mM $MgCl_2$, 10 mM HEPES, 0.2 EGTA, 2 mM MgATP, 0.5 mM NaGTP, and 5 mM biocytin (290 mOsm, adjusted to pH 7.3 with KOH). For recording GFP^- host cortical neurons, the patch electrodes were filled with solution containing 140 mM Cs-methanesulfonate, 5 mM NaCl, 1 mM $MgCl_2$, 10 mM HEPES, 0.2 EGTA, 2 mM MgATP, 0.5 mM NaGTP, 5 mM QX 314 chloride, and 5 mM biocytin (290 mOsm, adjusted to pH 7.3 with CsOH). The liquid junction potential of 15.5 and 8.9 mV was corrected for the K-gluconate-based and Cs-based pipette solutions, respectively. For experiments described in Figure 2c, whole-cell membrane capacitance (C_m) was compensated with the amplifier. Series (access) resistance was not compensated.

To calculate membrane resistance (R_m) and membrane capacitance (C_m) of grafted human interneurons in Supplementary Fig. 3b–c, we applied hyperpolarizing voltage pulses (–5 mV) from the holding voltage of –85 mV and recorded currents in voltage-clamp mode with a sampling rate of 100 kHz in GFP^+ grafted cells. The peak amplitude of the transient capacitive current (I_{peak}) was used to estimate apparent access resistance (R_a) using the equation, $R_a = –5\ mV / I_{peak}$. Steady-state current (I_{ss}) is the average current from the baseline for the last 5 ms of voltage pulse and was used to calculate membrane resistance (R_m) using the equation, $R_m = (–5\ mV / I_{ss}) – R_a$. Transient capacitive current was fitted with a double exponential function, $I(t) = I_f \exp(-t/\tau_f) + I_s \exp(-t/\tau_s)$, where I_f/τ_f and I_s/τ_s are the fast and slow components of peak amplitudes and the decay time constants for the transient capacitive current. The weighted mean decay time constant (τ_w) was calculated from the equation, $\tau_w = \tau_f [I_f/(I_f + I_s)] + \tau_s [I_s/(I_f + I_s)]$ and was then used to calculate membrane capacitance (C_m) from the equation, $C_m = \tau_w \times (R_a + R_m) / (R_a \times R_m)$.

To compare membrane excitability of grafted human cINs between groups (Figure 2d-e), the membrane potential was held at approximate –85 mV in current-clamp mode, and square pulses of depolarizing currents (10–90 pA with the increment of 10 pA, 0.5 s duration) were applied. The number of AP firings were counted for each current pulse in each grafted cell. The first AP induced by depolarizing current injection near threshold was used to calculate afterhyperpolarization (AHP), AP threshold, and AP half-width in Supplementary Fig. 3f–h. Spontaneous AP (sAP) firings were recorded in grafted interneurons in current-clamp mode without current injection or withdrawal for 2 minutes, and the average frequency of sAP firings was calculated for each grafted neuron (Figure 2f and Supplementary Fig. 3k). The resting membrane potential was estimated as the average membrane potential when the recorded graft cell did not fire APs spontaneously (Supplementary Fig. 3i).

Spontaneous EPSCs (sEPSC) were recorded in grafted human interneurons at −85 mV in voltage-clamp mode for 3–5 minutes (Figure 2g). The amplitude and frequency of sEPSC

were analyzed using the event detection function of the Clampfit software (Molecular Devices). The average amplitudes and frequencies of sEPSC were calculated for each grafted neuron and were compared between groups in Supplementary Fig. 5a–c. A blue collimated light-emitting diode (LED) with a 470 nm peak wavelength (M470L2, Thorlabs) was used for photostimulations of grafted interneurons expressing ChR2-GFP in Figure 2h-l and Supplementary Fig. 5d. Brain slices in the recording chamber were illuminated through a 40× water-immersion objective lens (Olympus LUMPLFLN 40XW or Leica HCX APO L40x #506155) and a 450–490 nm filter (Chroma). The illumination area was 0.17 mm^2 and was centered at the cell patched for recording.

After electrophysiological recordings, brain slices were fixed in 4 % paraformaldehyde at 4°C overnight. Recorded cells loaded with biocytin were labeled with streptavidin, Alexa 568 conjugate (20 μg/mL in PBS, Thermo Fisher Scientific) as described previously [51]. Images of biocytin/streptavidin-labelled cells were taken with the z-stack function using Leica a SP5 confocal microscope. Reagents were purchased from Tocris Bioscience (QX 314 chloride, biocytin, and NBQX) or Sigma-Aldrich (ATP, GTP, and SR95531). Offline analysis of electrophysiological data was performed using the Clampfit 9 program (Molecular Devices).

Electrophysiological analysis of iPSC-derived cINs *in vitro*

After 4 months' differentiation, human cINs were used for electrophygiological experiments. The cINs were transferred into a chamber continuously perfused (1.5–2 ml/min) with extracellular bath solution containing 140 mM NaCl, 2.8 mM KCl, 1.3 mM $NaHPO_4$, 10 mM dextrose, 1 mM $MgCl_2$, 2 mM $CaCl_2$, and 10 mM HEPES at pH 7.4 with osmolarity of 295–300mM. Recording pipettes with resistances of 4–6 MΩ were filled with an internal solution containing 120 mM K-gluconate, 9 mM KCl, 10 mM KOH, 8 mM NaCl, 10 mM HEPES, 3.48 mM MgATP, 0.4 mM Na_3GTP, 17.5 mM sucrose, and 0.5 mM EGTA, with an osmolarity of ~290 and pH 7.3. Whole-cell patch clamp recordings were performed at RT using a multiclamp 700B, digidata 1550, and Clampex 10 software (Molecular Devices). Sampling was done at 5 kHz. Liquid junction potential of 12.9 mV was corrected for the internal solution used. Resting membrane potential was recorded at I = 0. To compare membrane excitability, membrane potential was held at approximately –70 mV and square pulses of depolarizing current steps were applied in current-clamp mode (–10 – 80 pA in increments of 10 pA, 0.8s duration). The first AP induced by depolarizing current was used to analyze AP threshold, AHP, and AP half-width using Clampfit software (Molecular Devices). Averages ± SEM are represented in Supplementary Fig. 4. For the representative voltage clamp trace, cells were held at –70 mV and 800 ms duration square voltage pulses from –80 mV to –10 mV with increments of 10 mV were injected.

RNA-seq Analysis

For the pilot RNA-seq using 4 HC and 4 SCZ cINs, RNA quality was examined by the TapeStation 4200 (Agilent Technologies, Santa Clara, CA) and RNA concentration was determined using a Nanodrop (Thermo Fisher, Waltham, MA). Stranded cDNA libraries were prepared using TruSeq Stranded HT mRNA kits (Illumina, San Diego, CA) and sequenced on a NextSeq 500 (Illumina) in 75 bp paired-end mode. FASTQ files were

aligned to the human genome (assembly hg19) using STAR and GENCODE v19 transcriptome annotation. Read pairs aligned to gene features were counted and summarized as RPKM values at the gene-level using featureCount, taking into account the strandness of the reads and all transcript variants of each gene in the GENCODE annotation. Differentially expressed genes were determined using the voom-limma package in the Bioconductor R software.

RNA-seq data of six samples from postmortem tissues were obtained from GEO (accession number of GSE87194), including 3 HC (SRR4289084, SRR4289085, and SRR4289086) and 3 SCZ (SRR4289106, SRR4289107, and SRR4289109). QuickRNASeq pipeline [52] was used for pairwise correlation comparison.

For the RNA-seq of 14 HC and 14 SCZ cINs, RNA quality was examined by the Bioanalyzer 2100 (Agilent Technologies) and RNA concentration was determined by the Qubit Fluorometric Quantitation (Life Technologies). For each sample, 200–300ng of RNA was used to construct a cDNA sequencing library using the TruSeq Stranded mRNA Library Preparation Kit (Illumina), in accordance with the manufacturer's protocol using the poly-adenylated RNA isolation. Sequencing of paired-end reads (75 bp × 2) was performed in the Illumina NextSeq 550 system. Raw sequence reads were de-multiplexed and trimmed for adapters by using the Illumina bcl2fastq conversion software (v2.19). Sequence reads of each sample were pseudo-aligned to human hg38 reference transcriptome and the gene transcript abundance was quantified by using Kallisto. The differential expression of genes and transcripts were achieved by using the Sleuth and DESeq2 R packages. The Kallisto-Sleuth workflow and Kallisto-DESeq2 workflows are based upon a previous publication [53]. The RNA-seq data were deposited at the GEO < https://www.ncbi.nlm.nih.gov/geo/w> and the accession number is GSE118313 and GSE121376.

Genotype analysis

Samples from Dr. Cohen's laboratory were genotyped at the Broad Institute using the Illumina HumanOmniExpress-12v1 or the PsychChip 15048346 B manifest. QC was performed using PLINK 1.9 to retain variants with missingness <2% and exclude single nucleotide polymorphisms (SNPs) with excess heterozygosity (HardyWeinberg equilibrium $\chi 2$ P-values $<10^{-6}$). Genotype imputation was performed using a stepwise pre-phasing/imputation approach implemented by Eagle v2.3 and Minimac3. The 1000 Genomes Phase 3 data was used as a reference.

Samples from Dr. Weinberger's laboratory were genotyped at Lieber Institute for Brain Development. SNP genotyping with HumanHap650Y_V3 (N=135), Human 1M-Duo_V3 (N=357) and Omni5 (N=3) BeadChips (Illumina) was carried out according to the manufacturer's instructions with DNA extracted from cerebellar tissue. The genotype data were processed and normalized with the crlmm R/Bioconductor package [54] separately by platform. Genotype imputation was performed on high-quality observed genotypes (removing low quality and rare variants) using the prephasing/imputation stepwise approach implemented in IMPUTE2 [55] and Shape-IT [56], with the imputation reference set from the full 1000 Human Genomes Project Phase 3 data set, separately by platform. We retained common SNPs (MAF > 5%) that were present in the majority of the samples (missingness <

10%) that were in Hardy Weinberg equilibrium (at $p > 1\times10^{-6}$) using the Plink [57] version 1.9 tool kit [`plink --bfile $BFILE --geno 0.1 --maf 0.05 --hwe 0.000001`]. We then identified linkage disequilibrium (LD)-independent SNPs.

Transplantation of human cINs, Immunohistochemistry, and Synapse analysis

All animal protocols were approved by the Institutional Animal Care and Use Committee at McLean Hospital, New York Medical College, and University of California Riverside. Procedures were carried out in accordance with the approved guidelines. We have complied with all relevant ethical regulations. The cIN spheres were trypsinized on day 45 of differentiation, infected with LV-Syn-ChR2 (H134R)-GFP to facilitate optogenetic study and then treated with CultureOne (Invitrogen, 1:100) for a week. Eight weeks after differentiation, cells were trypsinized and resuspended in Transplantation media (HBSS, 4.5 mg/ml of sucrose, 0.1 ng/ml GDNF, 0.1 ng/ml BDNF, 0.02 μM Boc-Asp(OMe)-fluoromethyl ketone) at a concentration of 10^5 cells/μl and used for transplantation into the cortices of 5–7 weeks old male and female Nod Scid mice (Charles River Laboratory, Kingston, NY) under pentobarbital anesthesia (66mg/kg) using a Kopf stereotaxic instrument (Kopf, Tujunga, CA), equipped with a mouse adapter (Stoelting, Wood Dale, IL). A 1 μl volume of cells were injected at each of the following coordinates: AP −1.75 mm, L ±2.2 mm, V −2.0 mm; AP 0 mm, L ±3.8 mm, V −2.0 mm; AP +2.12 mm, L ±4.2 mm, V −1.8mm. Four months after transplantation, the mice were perfused with 0.1 M PBS followed by 4% paraformaldehyde (PFA). The brains were removed, and post-fixed in 4 % PFA solutions overnight and then placed in 30% sucrose solutions for 2 days. Forty-micrometer-thick coronal sections were cut on a freezing microtome (American Optical Corp., Buffalo, NY). The brain sections were blocked in PBS with 10% normal serum and 0.1% Triton X-100 for 10 min at RT and then incubated with primary antibody in PBS with 2% normal serum overnight at 4°C. After washing with PBS, the sections were incubated with the secondary antibody in PBS with 2% normal serum for 1 hour at RT. The antibodies used are summarized in Supplementary Table 1. Sections were visualized by the Confocal Leica TCS SP8 (Leica Microsystems, Buffalo Grove, IL) using sequential acquisition of separate channels with the 100X objective.

For synapse analysis, images were processed using Imaris software 9.2 (Bitplane, Switzerland), which allows objective counting of synaptic puncta based upon absolute fluorescent intensity. Synaptic puncta positive for VGAT (inhibitory presynaptic), Gephyrin (inhibitory postsynaptic), Vglut1 (excitatory presynaptic), PSD95 (excitatory postsynaptic) were identified with spot diameters of 0.5 μm. For inhibitory synapse analysis, only presynaptic $VGAT^+$ puncta that overlapped with GFP on confocal single plane images were included in the analysis, excluding all other $VGAT^+$ puncta. For postsynaptic excitatory puncta on cINs, only postsynaptic $PSD95^+$ puncta overlapped with GFP on confocal single plane images were included in the analysis. Synapse formation was determined by juxtaposition of GFP^+VGAT^+ puncta and $Gephyrin^+$ puncta for inhibitory synapses and GFP^+PSD95^+ puncta and $Vglut1^+$ puncta for excitatory synapses. The data were expressed as synapse numbers per GFP^+ neuronal surface area. For inhibitory synapse analysis, we analyzed a total of 835 neurite segments with a total area of 9,622 μm^2 for HC cINs and a total of 1,168 neurite segments with a total area of 13,611 μm^2 for SCZ cINs. Total counted

colocalized puncta numbers were 1,286 for HC cINs and 1,104 for SCZ cINs. For excitatory synapse analysis, we analyzed a total of 614 neurite segments with a total area of 11,732 μm^2 for HC cINs and a total of 669 neurite segments with a total area of 11,413 μm^2 for SCZ cINs. Total counted colocalized puncta numbers were 3,542 for HC cINs and 4,410 for SCZ cINs. The experimenters were blind to the sample ID during data collection.

iDISCO+ tissue-clearing and 3D imaging

To visualize the cIN grafts in 3D in mouse brains, we performed immunohistochemistry/tissue-clearing according to the iDISCO+ tissue clearing method [27]. The mouse was perfused with 0.1 M PBS followed by 4% PFA 4 months after transplantation. The brain was harvested and post-fixed in 4 % PFA solutions overnight. The mouse brain was dehydrated, bleached, rehydrated, and blocked as described [27]. The following antibodies were used for staining: mouse-anti-human cytoplasm (1:1,000, StemCells Inc. Newark, CA), and Alexa Fluor 568-conjugated donkey anti-mouse (1:1,000, Thermo Scientific). Solvent-cleared brain was imaged in its entirety with light-sheet microscopy (LaVision Ultramicroscope II Light Sheet, LaVision BioTec, Germany) at 2.5 X objective. Z-stack images taken from light-sheet microscopy were subjected to 3D rendering and spot analysis using Imaris software 9.2 (Bitplane).

Histological analysis of WT and *Pcdha* $^{\Delta\alpha/\Delta\alpha}$ mice

WT and *Pcdha* $^{\Delta\alpha/\Delta\alpha}$ mice were generated as described [58] and the mice were perfused at P40 for histological analysis. The mouse brains were post-fixed using a 4% PFA solution overnight and then placed in a 30% sucrose solution for 2 days. Forty-micrometer-thick coronal sections were cut by a microtome. Brain sections were blocked/permeabilized in PBS with 10% normal serum and 0.1% Triton X-100 for 10 min at RT and then incubated with an antibody against PV raised in rabbits (Swant, Bellinzona, Switzerland) in PBS with 2% normal serum overnight at 4°C. For amplification of signals, the sections were incubated with the biotinylated anti-rabbit antibody for 2 hours at RT, then followed by amplification steps as follows; Alexa568-streptavidin (1: 2,000, Life Technologies) for 2 hours at RT, then biotinylated anti-streptavidin antibody (1: 2,000, Vector) for 2 hours at RT and then incubated Alexa568- streptavidin for 2 hours at RT. Z-stack images were obtained using an Olympus DSU Spinning Disc Confocal on an IX81 inverted microscope. Arborization of WT vs *Pcdha* $^{\Delta\alpha/\Delta\alpha}$ PV$^+$ cINs was analyzed using Neuron J to obtain parameters such as neurite length, neurite number from the soma, and branch number within 150 μm from the cell body. The experimenters were blind to the sample ID during data collection.

The synapse analysis was performed using triple-stained WT or KO mice brain sections (PV/Gephyrin/VGAT or PV/VGlut1/PSD95) as described above. For inhibitory synapse analysis, we analyzed a total of 5,497 neurite segments with a total area of 55,186 μm^2 for WT cINs and a total of 4,733 neurite segments with a total area of 57,671 μm^2 for *Pcdha* $^{\Delta\alpha/\Delta\alpha}$ mice cINs. Total counted colocalized puncta numbers were 20,393 for WT and 12,097 for *Pcdha* $^{\Delta\alpha/\Delta\alpha}$ mice. For excitatory synapse analysis, we analyzed a total of 3,367 neurite segments with a total area of 30,394 μm^2 for WT cINs and a total of 3,648 neurite segments with a total area of 44,121 μm^2 for *Pcdha* $^{\Delta\alpha/\Delta\alpha}$ cINs. Total counted colocalized puncta

numbers were 9,655 for WT and 19,125 for *Pcdha* $^{\Delta\alpha/\Delta\alpha}$ mice. The experimenters were blind to the sample ID during data collection.

Prepulse inhibition (PPI) of *Pcdha* $^{\Delta CR/\Delta CR}$ or *Pcdha* $^{\Delta Bneo/\Delta Bneo}$ mice

All experiments were approved by the Institutional Animal Care and Use Committee at Osaka University. Procedures were carried out in accordance with the approved guidelines. We have complied with all relevant ethical regulations. We used 10–13 weeks old male *Pcdha* $^{\Delta CR/\Delta CR}$ mice and 10–13 weeks old male *Pcdha* $^{\Delta Bneo/\Delta Bneo}$ mice for behavior testing. The mice were maintained in groups of four per cage with a 12 h light/dark cycle and ad libitum access to food and water. *Pcdha* $^{\Delta CR/\Delta CR}$ mice and *Pcdha* $^{\Delta Bneo/\Delta Bneo}$ mice were established by backcrossing with C57BL/6 more than 8 times [24], and then used for PPI testing. A startle reflex measurement system was used (O'Hara &Co., Ltd). The background noise level was 70 dB in each chamber. Each mouse was placed in a Plexiglas tube for 5 min as an initial period of acclimation. The responses were recorded for 160 msec starting with the onset of the prepulse stimuli. The maximum startle amplitude scored during the 160 msec was used. Mice received a series of six trial types, two types for startle trials and three types for prepulse inhibition trials. The startle stimulus was a 110- or 120-dB sound. The prepulse sound was a 74-, 78- or 82-dB sound, which presented 100 ms before startle stimulus. These six trial types were presented in pseudorandom order and 10–20 sec intertrial intervals. The following formula was used to calculate percentage prepulse inhibition of ASR: (startle response for pulse alone - startle response for pulse with pre-pulse) / startle response for pulse alone) X 100.

Histological analysis of human postmortem tissue

Formalin-fixed PFC of human postmortem tissues from 8 HC and 8 SCZ were obtained from the McLean Hospital, the University of Maryland Brain and Tissue Bank, the University of Pittsburgh, and the Human Brain and Spinal Fluid Resource Center (Figure 8a). The tissue samples were placed in a 30% sucrose solution for 2 days. Forty-micrometer-thick coronal sections were cut using a cryostat (Leica). The brain sections were blocked in PBS with 10% normal serum and 0.1% Triton X-100 for 10 min at RT and then incubated with primary antibody in PBS with 2% normal serum overnight at 4°C. After washing with PBS, the sections were incubated with the secondary antibody in PBS with 2% normal serum for 1 hour at RT. The sections were incubated in a solution containing 0.01M CuSO4 (Sigma) and 0.05 M Ammonium acetate (Sigma) for 2 min at RT and then washed with PBS 5 times. For arborization analysis, Z-stack images of layer 3 PV^+ neurons were taken using the EVOS FL Auto microscope (Life Technologies) and analyzed using Neuron J to obtain parameters such as neurite length, neurite number from the soma, and branch number within 150 μm of the cell body. The experimenters were blind to the sample ID during data collection.

For synapse analysis, synaptic puncta images of layer 3 PV^+ neurons were taken using a LSM 710 confocal microscope (Carl Zeiss, Germany) using sequential acquisition of separate channels with the 100X objective. For inhibitory synapse analysis, we analyzed a total of 7,471 neurite segments with a total area of 57,218 μm^2 for HC postmortem tissue and a total of 7,644 neurite segments with a total area of 68,563 μm^2 for SCZ postmortem

tissue. Total counted colocalized puncta numbers were 14,562 for HC postmortem tissue and 13,113 for SCZ postmortem tissue. For excitatory synapse analysis, we analyzed a total of 9,051 neurite segments with a total area of 111,301 μm^2 for HC postmortem tissue and a total of 4,240 neurite segments with a total area of 31,165.3 μm^2 for SCZ postmortem tissue. Total counted colocalized puncta numbers were 27,086 for HC postmortem tissue and 4,822 for SCZ postmortem tissue. The experimenters were blind to the sample ID during data collection.

Statistical analysis

All statistical analyses were performed using GraphPad Prism7 (GraphPad Software, La Jolla, CA), SPSS (version 16; SPSS Inc., Chicago, IL) and SAS statistical software (9.4, SAS Institute, Cary, NC). We tested normality of data distribution as summarized in Supplementary Tables 15–18. For cell counting analysis (Figure 1 and Supplementary Fig. 1), one-way ANOVA was used to analyze the differences among group means of individual cell lines. For in vitro electrophysiology data (Supplementary Fig. 4), Welch's t-test was used to compare the mean difference between groups. For mice behavioral assessments (Figure 5d-e), the data were analyzed by the two-tailed unpaired t-test. For real time PCR analysis of siRNA-mediated gene KD (Supplementary Fig. 10c), the data were analyzed by two-tailed unpaired t-test.

For phenotype analysis such as in vivo electrophysiology data (Figure 2, Supplementary Fig. 3 and 5, and Supplementary Table 15), gene expression analysis (Figure 3–4, Supplementary Fig. 8, and Supplementary Table 16), synapse analysis (Figure 5b–c, Figure 7f-g, Figure 8c-d, and Supplementary Table 17) and arborization analysis (Figure 5a, Figure 6a, Figure 8b, and Supplementary Table 17), the linear mixed effect model with random intercept was used for the continuous data and the mixed effects log-linear model with random intercept was used for count data to compare the mean difference between groups [59,60]. Mixed model methods were chosen to handle clustering and covariance among correlated samples. Some of the data were log-transformed to deal with skewedness as indicated in Supplementary table 15–18. Power analysis (Figure 2l) was performed using the tests for two means in a cluster design to incorporate the clustering of samples within the same lines. For arborization analysis after GO6893 treatment (Figure 6b and Supplementary Table 17), the two-level hierarchical mixed effects models were used by incorporating the two random effects (i.e., the second effect is for observations with and without GO6893 nested within the first effect, same batch of cells) to account for correlation among the paired samples in each cell line. For arborization analysis after siRNA transfection (Figure 6c and Supplementary Table 18), the two-level hierarchical linear mixed effect model for the continuous data and the two-level hierarchical mixed effect log-linear model for the count data were used. Dunnett's test was used to compare each of groups with a negative control siRNA control group as a post hoc analysis with an adjustment for multiple comparisons. A two-sided significance level of 5% was used for all analyses. More information on statistical analysis can be found in the Life Sciences Reporting Summary.

Study design

No statistical method was used to pre-determine sample sizes. However, the sample size we used in this study is similar to the largest one among previous publications [61]. This sample size was adequate in identifying the disruption of protocadherin expression in SCZ cINs. No data was excluded from analysis. Experimental cohorts were chosen based on our selection criteria (Caucasian male patients treated with Clozapine vs. age- and gender-matched Caucasian male healthy controls) without randomization to reduce variation caused by age, ethnicity and gender. Blinding was used during cell counting, arborization analysis and synapse analysis.

Life Sciences Reporting Summary

Further information on experimental design is available in the Life Sciences Reporting Summary.

Supplementary Material

Refer to Web version on PubMed Central for supplementary material.

Acknowledgement

We thank G. Genovese of Program in Medical and Population Genetics at Broad Institute of MIT and Harvard for providing consultation with genotype analysis. We thank S. Berretta at McLean Hospital/Harvard Medical School for her expert advice and help with human postmortem tissue study. We thank NIH Neurobiobank for providing human postmortem tissues. The authors are appreciative of the New York Medical College/Westchester Medical Center Translational Stem Cell Center for its support with confocal imaging. This study was supported by NIH MH107884 (S.C.), NYSTEM C32607GG (S.C.), Japan Society for the Promotion of Science (JSPS) KAKENHI grant JP17K01976 (T.H.), JSPS grant 16H01275 (T.Y.), AMED-CREST (T.Y.), the Initial Complement Funds from the University of California Riverside (J.-H.C.), NIH MH113894 (J.-H.C.) and NIH MH118339 (J.-H.C.).

References

1. Sullivan PF, Kendler KS & Neale MC Schizophrenia as a complex trait: evidence from a meta-analysis of twin studies. Archives of general psychiatry 60, 1187–1192 (2003). [PubMed: 14662550]
2. Weinberger DR Implications of normal brain development for the pathogenesis of schizophrenia. Archives of general psychiatry 44, 660–669 (1987). [PubMed: 3606332]
3. Buchanan RW & Carpenter WT Domains of psychopathology: an approach to the reduction of heterogeneity in schizophrenia. The Journal of nervous and mental disease 182, 193–204 (1994). [PubMed: 10678315]
4. Elvevag B & Goldberg TE Cognitive impairment in schizophrenia is the core of the disorder. Critical reviews in neurobiology 14, 1–21 (2000). [PubMed: 11253953]
5. Ripke S, et al. Biological Insights From 108 Schizophrenia-Associated Genetic Loci. Nature 511, 421–427 (2014). [PubMed: 25056061]
6. Fromer M, et al. Gene expression elucidates functional impact of polygenic risk for schizophrenia. Nature neuroscience 19, 1442–1453 (2016). [PubMed: 27668389]
7. Sekar A, et al. Schizophrenia risk from complex variation of complement component 4. Nature 530, 177–183 (2016). [PubMed: 26814963]
8. Takahashi K & Yamanaka S Induction of pluripotent stem cells from mouse embryonic and adult fibroblast cultures by defined factors. Cell 126, 663–676 (2006). [PubMed: 16904174]
9. Brennand KJ, et al. Modelling schizophrenia using human induced pluripotent stem cells. Nature 473, 221–225 (2011). [PubMed: 21490598]

10. Noh H, Shao Z, Coyle JT & Chung S Modeling schizophrenia pathogenesis using patient-derived induced pluripotent stem cells (iPSCs). Biochimica et biophysica acta 1863, 2382–2387 (2017). [PubMed: 28668333]
11. Benes FM The GABA system in schizophrenia: cells, molecules and microcircuitry. Schizophrenia research 167, 1–3 (2015). [PubMed: 26255083]
12. Lewis DA, Hashimoto T & Volk DW Cortical inhibitory neurons and schizophrenia. Nature reviews. Neuroscience 6, 312–324 (2005). [PubMed: 15803162]
13. Volk DW & Lewis DA Early developmental disturbances of cortical inhibitory neurons: contribution to cognitive deficits in schizophrenia. Schizophrenia bulletin 40, 952–957 (2014). [PubMed: 25053651]
14. Lewis DA, et al. Subunit-selective modulation of GABA type A receptor neurotransmission and cognition in schizophrenia. The American journal of psychiatry 165, 1585–1593 (2008). [PubMed: 18923067]
15. Belforte JE, et al. Postnatal NMDA receptor ablation in corticolimbic interneurons confers schizophrenia-like phenotypes. Nature neuroscience 13, 76–83 (2010). [PubMed: 19915563]
16. Warren L, Ni Y, Wang J & Guo X Feeder-free derivation of human induced pluripotent stem cells with messenger RNA. Scientific reports 2, 657 (2012). [PubMed: 22984641]
17. Kim TG, et al. Efficient specification of interneurons from human pluripotent stem cells by dorsoventral and rostrocaudal modulation. Stem cells (Dayton, Ohio) 32, 1789–1804 (2014).
18. Ma T, et al. Subcortical origins of human and monkey neocortical interneurons. Nature neuroscience 16, 1588–1597 (2013). [PubMed: 24097041]
19. Zhang Y, et al. Rapid single-step induction of functional neurons from human pluripotent stem cells. Neuron 78, 785–798 (2013). [PubMed: 23764284]
20. Hasegawa S, et al. Distinct and Cooperative Functions for the Protocadherin-alpha, -beta and -gamma Clusters in Neuronal Survival and Axon Targeting. Frontiers in molecular neuroscience 9, 155 (2016). [PubMed: 28066179]
21. Hirayama T & Yagi T Clustered protocadherins and neuronal diversity. Progress in molecular biology and translational science 116, 145–167 (2013). [PubMed: 23481194]
22. Swerdlow NR, et al. Startle gating deficits in a large cohort of patients with schizophrenia: relationship to medications, symptoms, neurocognition, and level of function. Archives of general psychiatry 63, 1325–1335 (2006). [PubMed: 17146007]
23. Katori S, et al. Protocadherin-alpha family is required for serotonergic projections to appropriately innervate target brain areas. The Journal of neuroscience : the official journal of the Society for Neuroscience 29, 9137–9147 (2009). [PubMed: 19625505]
24. Fukuda E, et al. Down-regulation of protocadherin-alpha A isoforms in mice changes contextual fear conditioning and spatial working memory. The European journal of neuroscience 28, 1362–1376 (2008). [PubMed: 18973563]
25. Garrett AM, Schreiner D, Lobas MA & Weiner JA gamma-protocadherins control cortical dendrite arborization by regulating the activity of a FAK/PKC/MARCKS signaling pathway. Neuron 74, 269–276 (2012). [PubMed: 22542181]
26. Southwell DG, et al. Interneurons from embryonic development to cell-based therapy. Science (New York, N.Y.) 344, 1240622 (2014).
27. Renier N, et al. iDISCO: a simple, rapid method to immunolabel large tissue samples for volume imaging. Cell 159, 896–910 (2014). [PubMed: 25417164]
28. Mayer C, et al. Developmental diversification of cortical inhibitory interneurons. Nature 555, 457–462 (2018). [PubMed: 29513653]
29. Phillips GR, et al. Gamma-protocadherins are targeted to subsets of synapses and intracellular organelles in neurons. The Journal of neuroscience : the official journal of the Society for Neuroscience 23, 5096–5104 (2003). [PubMed: 12832533]
30. Wang X, et al. Gamma protocadherins are required for survival of spinal interneurons. Neuron 36, 843–854 (2002). [PubMed: 12467588]
31. Bonn S, Seeburg PH & Schwarz MK Combinatorial expression of alpha- and gamma-protocadherins alters their presenilin-dependent processing. Molecular and cellular biology 27, 4121–4132 (2007). [PubMed: 17403907]

32. Murata Y, Hamada S, Morishita H, Mutoh T & Yagi T Interaction with protocadherin-gamma regulates the cell surface expression of protocadherin-alpha. The Journal of biological chemistry 279, 49508–49516 (2004). [PubMed: 15347688]
33. Chen J, et al. alpha- and gamma-Protocadherins negatively regulate PYK2. The Journal of biological chemistry 284, 2880–2890 (2009). [PubMed: 19047047]
34. Lu WC, et al. The protocadherin alpha cluster is required for axon extension and myelination in the developing central nervous system. Neural regeneration research 13, 427–433 (2018). [PubMed: 29623926]
35. Morishita H, et al. Myelination triggers local loss of axonal CNR/protocadherin alpha family protein expression. The European journal of neuroscience 20, 2843–2847 (2004). [PubMed: 15579137]
36. Kohmura N, et al. Diversity revealed by a novel family of cadherins expressed in neurons at a synaptic complex. Neuron 20, 1137–1151 (1998). [PubMed: 9655502]
37. Hirayama T & Yagi T Regulation of clustered protocadherin genes in individual neurons. Seminars in cell & developmental biology 69, 122–130 (2017). [PubMed: 28591566]
38. Jones CA, Watson DJ & Fone KC Animal models of schizophrenia. British journal of pharmacology 164, 1162–1194 (2011). [PubMed: 21449915]
39. Pak C, et al. Human Neuropsychiatric Disease Modeling using Conditional Deletion Reveals Synaptic Transmission Defects Caused by Heterozygous Mutations in NRXN1. Cell stem cell 17, 316–328 (2015). [PubMed: 26279266]
40. Southwell DG, et al. Intrinsically determined cell death of developing cortical interneurons. Nature 491, 109–113 (2012). [PubMed: 23041929]
41. Franco R & Cedazo-Minguez A Successful therapies for Alzheimer's disease: why so many in animal models and none in humans? Frontiers in pharmacology 5, 146 (2014). [PubMed: 25009496]
42. Thomsen MS, Hansen HH, Timmerman DB & Mikkelsen JD Cognitive improvement by activation of alpha7 nicotinic acetylcholine receptors: from animal models to human pathophysiology. Current pharmaceutical design 16, 323–343 (2010). [PubMed: 20109142]
43. Amrollahi Z, et al. Double-blind, randomized, placebo-controlled 6-week study on the efficacy and safety of the tamoxifen adjunctive to lithium in acute bipolar mania. Journal of affective disorders 129, 327–331 (2011). [PubMed: 20843556]
44. Bebchuk JM, et al. A preliminary investigation of a protein kinase C inhibitor in the treatment of acute mania. Archives of general psychiatry 57, 95–97 (2000). [PubMed: 10632242]
45. Yildiz A, Guleryuz S, Ankerst DP, Ongur D & Renshaw PF Protein kinase C inhibition in the treatment of mania: a double-blind, placebo-controlled trial of tamoxifen. Archives of general psychiatry 65, 255–263 (2008). [PubMed: 18316672]
46. Forstner AJ, et al. Identification of shared risk loci and pathways for bipolar disorder and schizophrenia. PloS one 12, e0171595 (2017). [PubMed: 28166306]
47. Chung DW, Fish KN & Lewis DA Pathological Basis for Deficient Excitatory Drive to Cortical Parvalbumin Interneurons in Schizophrenia. The American journal of psychiatry 173, 1131–1139 (2016). [PubMed: 27444795]
48. Roberts RC, Barksdale KA, Roche JK & Lahti AC Decreased synaptic and mitochondrial density in the postmortem anterior cingulate cortex in schizophrenia. Schizophrenia research 168, 543–553 (2015). [PubMed: 26210550]
49. Akbarian S & Huang HS Molecular and cellular mechanisms of altered GAD1/GAD67 expression in schizophrenia and related disorders. Brain research reviews 52, 293–304 (2006). [PubMed: 16759710]
50. Bliss LA, et al. Use of postmortem human dura mater and scalp for deriving human fibroblast cultures. PloS one 7, e45282 (2012). [PubMed: 23028905]
51. Cho JH, Deisseroth K & Bolshakov VY Synaptic encoding of fear extinction in mPFC-amygdala circuits. Neuron 80, 1491–1507 (2013). [PubMed: 24290204]
52. Zhao S, et al. QuickRNASeq lifts large-scale RNA-seq data analyses to the next level of automation and interactive visualization. BMC genomics 17, 39 (2016). [PubMed: 26747388]

53. Bray NL, Pimentel H, Melsted P & Pachter L Near-optimal probabilistic RNA-seq quantification. Nature biotechnology 34, 525–527 (2016).

54. Scharpf RB, Irizarry RA, Ritchie ME, Carvalho B & Ruczinski I Using the R Package crlmm for Genotyping and Copy Number Estimation. Journal of statistical software 40, 1–32 (2011).

55. Howie BN, Donnelly P & Marchini J A flexible and accurate genotype imputation method for the next generation of genome-wide association studies. PLoS genetics 5, e1000529 (2009). [PubMed: 19543373]

56. Delaneau O, Coulonges C & Zagury JF Shape-IT: new rapid and accurate algorithm for haplotype inference. BMC bioinformatics 9, 540 (2008). [PubMed: 19087329]

57. Purcell S, et al. PLINK: a tool set for whole-genome association and population-based linkage analyses. American journal of human genetics 81, 559–575 (2007). [PubMed: 17701901]

58. Hasegawa S, et al. The protocadherin-alpha family is involved in axonal coalescence of olfactory sensory neurons into glomeruli of the olfactory bulb in mouse. Molecular and cellular neurosciences 38, 66–79 (2008). [PubMed: 18353676]

59. Herring AH Applied Longitudinal Analysis, 2nd Edition, by Fitzmaurice Garrett M., Laird Nan M., and Ware James H., John Wiley & Sons, 2011. Journal of Biopharmaceutical Statistics 23, 940–941 (2013).

60. Laird NM & Ware JH Random-effects models for longitudinal data. Biometrics 38, 963–974 (1982). [PubMed: 7168798]

61. Topol A, et al. Dysregulation of miRNA-9 in a Subset of Schizophrenia Patient-Derived Neural Progenitor Cells. Cell reports 15, 1024–1036 (2016). [PubMed: 27117414]

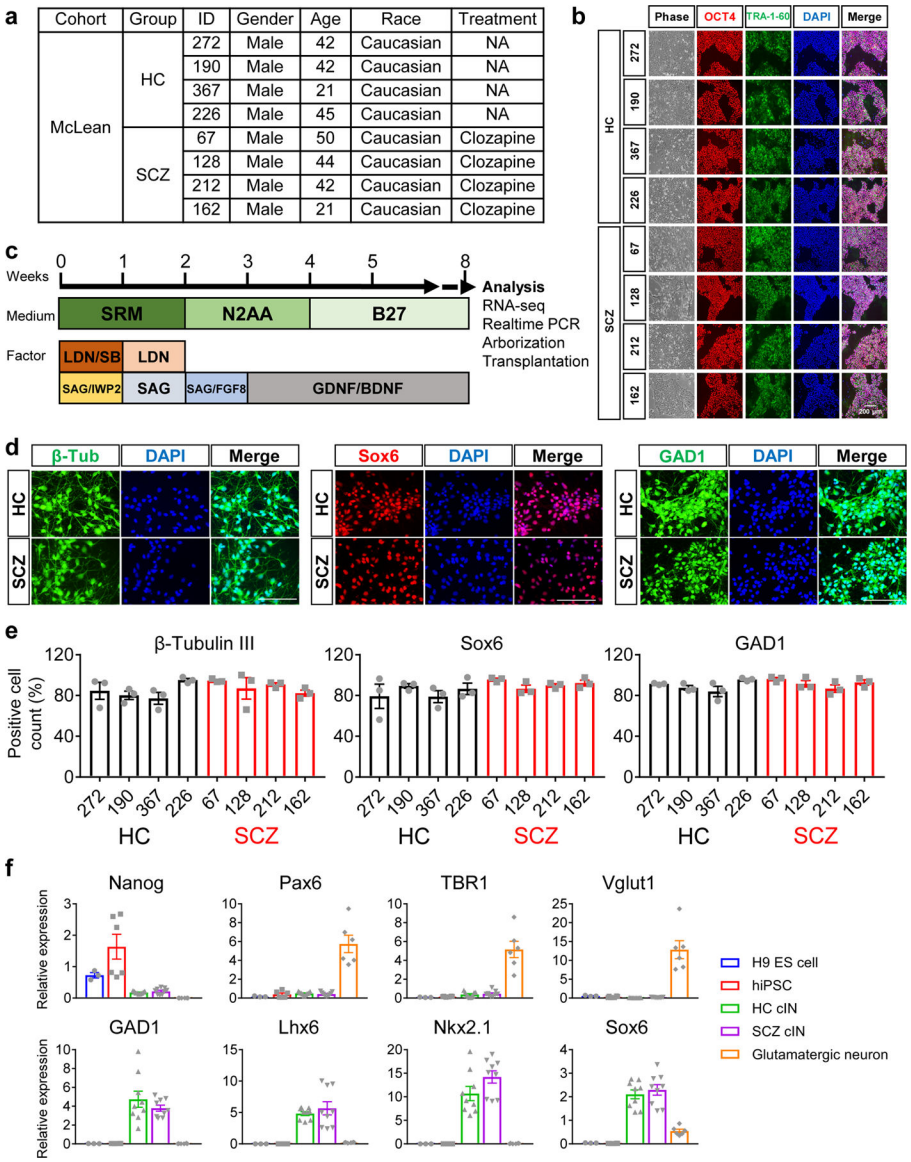

Figure 1. SCZ and HC iPSCs efficiently generate homogeneous population of cINs.

The lines used in each experiment are summarized in Supplementary Table 3.

(a) Table of subjects analyzed in pilot study.

(b) Immunocytochemistry analysis of human PSC markers, Oct4 and Tra-1–60, in generated iPSCs (Scale bar = 200 μm). Differentiation was repeated at least 3 times with comparable results.

(c) Differentiation scheme of cINs from human iPSCs. SRM: serum replacement media, LDN: 100 nM LDN193189, SB: 10 μM SB431542, SAG: 0.1 μM Smoothened agonist, and IWP2: 5 μM Inhibitor of Wnt production-2.

(d) Immunocytochemistry analysis for expression of β-Tubulin III, Sox6, and GAD1 in generated cINs after 8 weeks' differentiation (Scale bar = 50 μm). Differentiation was repeated at least 3 times with comparable results.

(e) Cell counting analysis after 8 weeks' differentiation. Data are presented as mean ±SEM from three independent differentiations (n = 3 differentiations). There were no significant differences among different lines based on one-way ANOVA (β-Tubulin III $p = 0.2626$, Sox6 $p = 0.3802$, and GAD1 $p = 0.5072$).

(f) Real-time PCR analysis of different cell types (H9 hESC: n = 3 batches, hiPSC: n = 6 batches from 2 iPSC lines, HC cIN: n = 9 batches from 3 lines, SCZ cIN: n = 9 batches from 3 lines, and glutamatergic neuron: n = 6 batches from 2 lines). Results were normalized using Glyceraldehyde-3-Phosphate Dehydrogenase (GAPDH) expression levels and presented as mean ±SEM.

See also Supplementary Fig. 1–2.

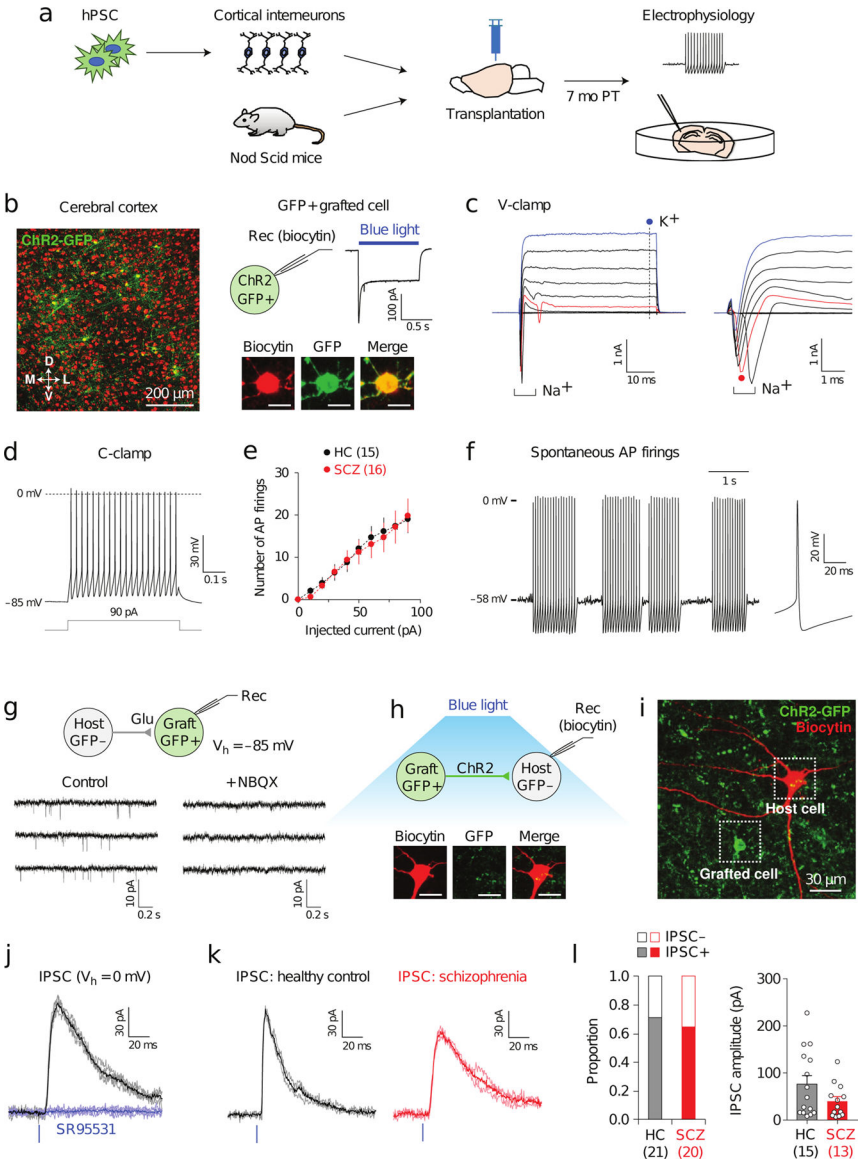

Figure 2. Neuronal and synaptic properties of cINs transplanted into mouse cerebral cortex.

The lines used in each experiment are summarized in supplementary Table 3.

(a) Transplantation scheme of cINs into Nod Scid mice. Eight-week old cINs infected with LV-Syn-ChR2-GFP were transplanted into cerebral cortices. Brain slices were prepared for electrophysiological experiments 7 months after grafting.

(b) *Left*: image showing ChR2-GFP-expressing grafted cINs (green) in the cerebral cortex. *Right*: patch-clamp recordings were performed with grafted cells, which generated ChR2-mediated photocurrents and were labeled with biocytin-streptavidin-Alexa 568 (scale bar = 10 μm).

(c) Voltage pulses from –115 mV to 85 mV with 20 mV increments induced transient inward (Na^+) and sustained outward currents (K^+) in a grafted cINs. Na^+ currents were quantified as peak inward currents induced by depolarization to –35 mV (red). K^+ currents were quantified as sustained outward currents induced by depolarization to 85 mV (blue).

(d) AP firing induced by current injection in a grafted cell at approximately –85 mV.
(e) Summary plot of AP firings in transplanted cINs in the HC (15 cells) and SCZ groups (16 cells). Repeated measures two-way ANOVA was used for analysis (Main effect of groups, $p = 0.77$; group × current interaction, $p = 1.00$). Error bars are the SEM.
(f) *Left*: spontaneous AP firings recorded at RMP in a grafted cIN. *Right*: average AP firings.
(g) Spontaneous EPSCs recorded in a grafted cell at –85 mV (left) and blocked by NBQX (right).
(h) Photostimulation activates ChR2-expressing grafted cINs, generating IPSCs in GFP^- host neurons labeled with biocytin (red, scale bar = 10 μm).
(i) Image showing a GFP^+ grafted human cIN (green) and a GFP^- host cortical neuron labeled with biocytin (red).
(j) Photostimulation induced IPSCs recorded at 0 mV in a host neuron (black) and inhibited by SR95531 (10 mM, blue).
(k) IPSCs induced by photostimulations (40 mW/mm^2) and recorded in host neurons in the HC (black) and SCZ groups (red).
(l) *Left*: comparison of the proportion of host cells with IPSCs in the HC (15 cells out of 21 cells examined) and SCZ groups (13 cells our of 20 cells examined; $p = 0.66$, $\chi 2$ test). *Right*: comparison of IPSC amplitude in the HC (15 cells) and SCZ groups (13 cells; $p = 0.37$). Error bars are the SEM.
See also Supplementary Fig. 3–5. For detailed statistics information, see Supplementary Table 15.

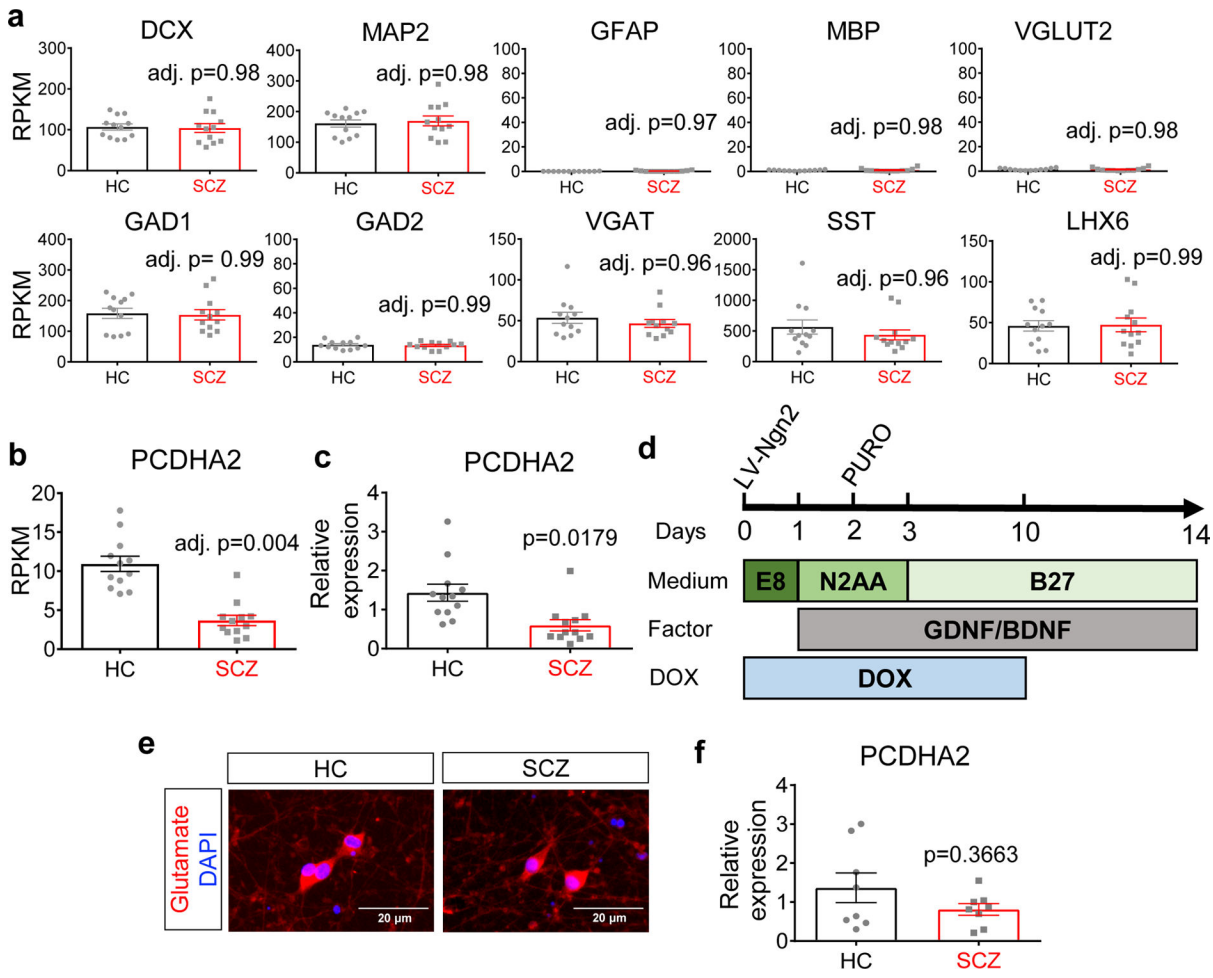

Figure 3. *PCDHA2* expression is significantly altered in developing SCZ cINs.

The lines used in each experiment are summarized in Supplementary Table 3. The breakdown data are summarized in Supplementary Table 4–5.

(a) RNA-seq transcriptome profiling of cINs derived from 4 HC vs. 4 SCZ iPSCs in three independent differentiations (n = 12 differentiations). Gene expression is shown as reads per kilobase of transcript per million mapped reads (RPKM). Differential expression was analyzed in R by the Voom function in Limma with adjusted multiple testing. Center and error bars show mean ± SEM.

(b) *PCDHA2* expression is significantly decreased in SCZ cINs. Data were collected by RNA-seq transcriptome profiling of cINs derived from 4 HC vs. 4 SCZ iPSCs in three independent differentiations (n = 12 differentiations). Differential expression was analyzed in R by the Voom function in Limma with adjusted multiple testing. Center and error bars show mean ± SEM.

(c) Quantitative real-time PCR analysis of *PCDHA2* expression in cINs derived from 4 HC iPSCs vs. 4 SCZ iPSCs in three independent differentiations (n = 12 differentiations). Data were normalized by GAPDH expression level. Center and error bars show mean ± SEM.

(d) The differentiation scheme for glutamatergic neurons. Human iPSCs were plated with Lentivirus expressing inducible Ngn2-puroR and treated with Doxycycline (DOX) until day 10. Cells were treated with Puromycin on day 2 and were used for analysis on day 14.

(e) Immunocytochemistry analysis of iPSC-derived glutamatergic neurons (scale bar = 20 μm). This analysis was repeated in 2 batches of differentiation with similar results.
(f) Quantitative real-time PCR analysis of *PCDHA2* expression in glutamatergic neurons derived from 4 HC vs. 4 SCZ iPSCs in two independent differentiations (n = 8 differentiations). *PCDHA2* expression level was normalized using that of GAPDH. Center and error bars show mean ± SEM.
See also Supplementary Fig. 6–7. For detailed statistics information, see Supplementary Table 15.

a

HC						SCZ					
Cohort	ID	Gender	Age	Race	Treatment	Cohort	ID	Gender	Age	Race	Treatment
McLean	317	Male	51	Caucasian	NA	McLean	67	Male	50	Caucasian	Clozapine
	PYUAM	Male	26	Caucasian	NA		117	Male	27	Caucasian	Clozapine
	272	Male	42	Caucasian	NA		128	Male	44	Caucasian	Clozapine
	190	Male	42	Caucasian	NA		212	Male	42	Caucasian	Clozapine
	367	Male	21	Caucasian	NA		162	Male	21	Caucasian	Clozapine
	292	Male	43	Caucasian	NA		58	Male	43	Caucasian	Clozapine
	365	Male	52	Caucasian	NA		282	Male	51	Caucasian	Clozapine
	226	Male	45	Caucasian	NA		285	Male	47	Caucasian	Clozapine
	M_139	Male	20	Caucasian	NA	NIMH	483	Male	39	Caucasian	Clozapine
MGH	99	Male	32	Caucasian	NA		689	Male	32	Caucasian	Clozapine
	107	Male	27	Caucasian	NA		755	Male	32	Caucasian	Clozapine
Lieber	L5	Male	54	Caucasian	NA		1442	Male	26	Caucasian	Clozapine
	L7	Male	25	Caucasian	NA	Lieber	L8	Male	50	Caucasian	Clozapine
	L9	Male	38	Caucasian	NA		L10	Male	37	Caucasian	Clozapine

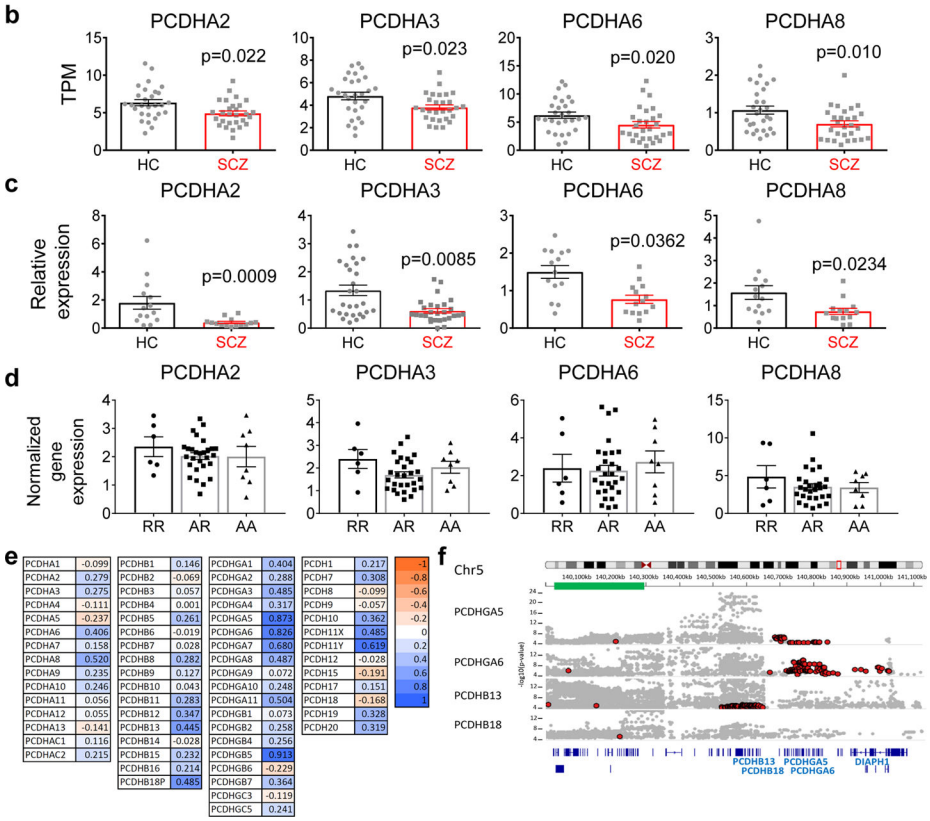

Figure 4. Multiple *PCDHA* family members are affected in developing SCZ cINs.

The lines used in each experiment are summarized in Supplementary Table 3. The breakdown data are summarized in Supplementary Table 6.

(a) Table of subjects in the expanded cohort.

(b) Changes in multiple *PCDHA* gene expression, analyzed by RNA-seq of cINs derived from 14 HC vs. 14 SCZ iPSCs in two independent differentiations (n = 28 differentiations). Expression level was shown as transcripts per kilobase million (TPM). Differentially expressed genes were analyzed by DESeq2 and Sleuth (Wald test for significance testing). Center and error bars show mean ± SEM.

(c) Quantitative real-time PCR analysis of expression of multiple *PCDHA* family members in cINs derived from 14 HC vs. 14 SCZ iPSCs in two independent differentiations (n = 28 differentiations). The expression levels of each gene were normalized by that of the GAPDH gene. Center and error bars show mean ± SEM.

(d) Correlation between genotype and gene expression level. R designates reference allele (G) and A designates alternate allele (A) of rs7445192. Gene expression levels were normalized by β-actin and grouped by genotype. The difference between the RR group and the AA group was analyzed by the two-tailed unpaired t-test (n = 6 for RR and n = 8 for AA; *PCDHA2* p = 0.5102, *PCDHA3* p = 0.4551, *PCDHA6* p = 0.7251 and *PCDHA8* p = 0.3548). Center and error bars show mean ± SEM.

(e) Heat map depicting expression changes of protocadherin genes in SCZ cINs. Blue color depicts downregulation in SCZ cINs and red depicts upregulation. Numbers in colored box indicate expression change in log2 fold change.

(f) eQTL diagram of different protocadherin genes, showing the presence of multiple eQTLs for protocadherin family members within SCZ risk loci. Green bar designates SCZ risk loci (Chr5: 140,023,664–140,222,664). Red dots are significant cis-eQTLs for the given gene at FDR<5%. More detailed information on this analysis can be found in the Commonmind portal (https://www.synapse.org/#!Synapse:syn2759792/wiki/69613).

See also Supplementary Fig. 8. For detailed statistics information, see Supplementary Table 16.

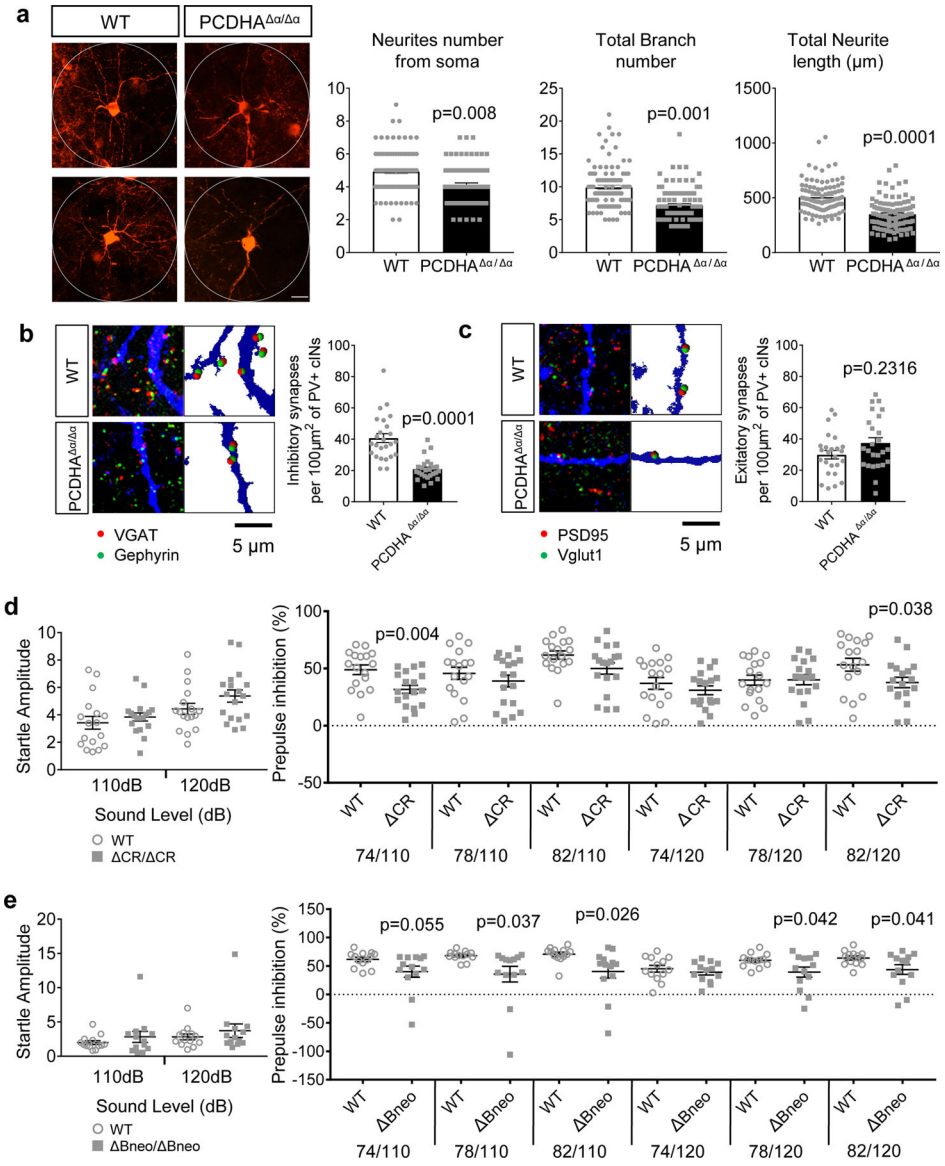

Figure 5. *Pcdha* KO (*Pcdha* $^{\Delta\alpha/\Delta\alpha}$) leads to cIN abnormalities in the PFC and behavioral abnormalities.

The breakdown data for each mouse are summarized in Supplementary Table 7–8.

(a) Arborization analysis of PV^+ cINs in PFC of littermate wildtype (WT) or *Pcdha* KO (*Pcdha* $^{\Delta\alpha/\Delta\alpha}$) mice. Arborization within 150 μm of the cell body was traced and analyzed using ImageJ with the Neuron J plugin and is presented as mean ±SEM (n = 100 neurons per group).

(b-c) Analyses of inhibitory and excitatory synapses in PFC of WT and *Pcdha* $^{\Delta\alpha/\Delta\alpha}$ mice using Imaris software. For inhibitory synapse analysis on PV^+ cINs, the data are presented as the number of inhibitory synapses (juxtaposed PV^+VGAT^+ puncta and $Gephyrin^+$ puncta) per 100 μm^2 of PV^+ cINs. For excitatory synapse analysis on PV^+ cINs, the data are presented as the number of excitatory synapses (juxtaposed PV^+PSD95^+ puncta and $Vglut1^+$ puncta) per 100 μm^2 of PV^+ cINs. Data are presented as mean ±SEM (n = 25 116 μm × 116 μm images per group).

(d) *Pcdha* $^{\Delta CR/\Delta CR}$ mice show a deficit in PPI. Amplitudes of startle response and percentage of PPI are shown. The data were analyzed using the two-tailed unpaired t-test. Data are shown as mean ±SEM (WT: n = 17 mice, ΔCR: n = 18 mice).

(e) *Pcdha* $^{\Delta Bneo/\Delta Bneo}$ mice show a deficit in PPI. Amplitudes of the startle response and the percentage of PPI are shown. The data were analyzed using the two-tailed unpaired t-test. Data are shown as mean ±SEM for the indicated numbers of mice (n = 13 mice for each group).

See also Supplementary Fig. 9. For detailed statistics information, see Supplementary Table 17.

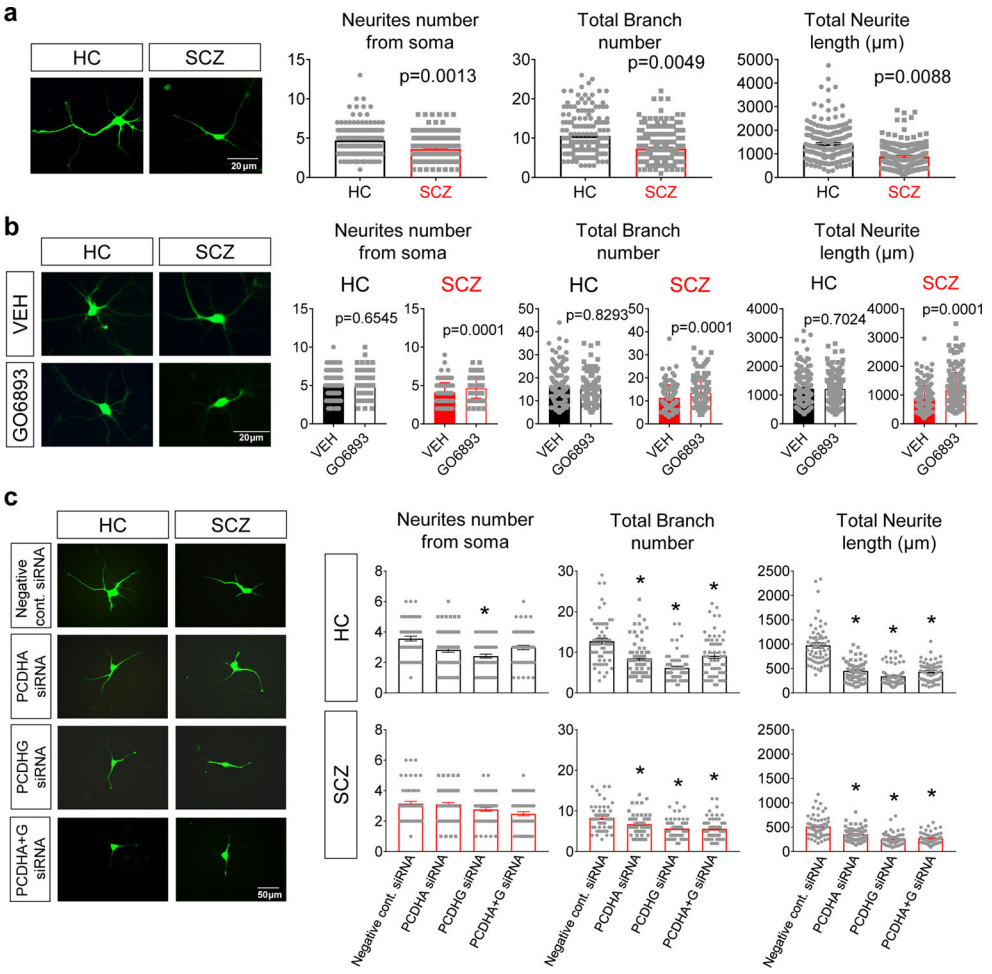

Figure 6. Developing SCZ cINs show arborization deficit relevant to protocadherin dysregulation *in vitro*.

The lines used in each experiment are summarized in Supplementary Table 3. The breakdown data for each line are summarized in Supplementary Tables 9–11.

(a) Arborization analysis of HC vs. SCZ cINs infected with a limiting titer of GFP-expressing lentivirus. Images were analyzed using ImageJ with the Neuron J plugin. (n = 180 neurons). Center and error bars show mean ± SEM.

(b) Arborization analysis of PKC inhibitor-treated HC vs. SCZ cINs. cINs infected with a limiting titer of GFP-expressing lentivirus were treated with PKC inhibitor GO6893 for 12 days and analyzed using ImageJ with the Neuron J plugin (n = 160 neurons). Center and error bars show mean ± SEM.

(c) Arborization analysis of siRNA transfected HC vs. SCZ cINs (two independent differentiations). cINs infected with a limiting titer of GFP-expressing lentivirus were transfected with siRNA against *PCDHA, PCDHG*, or a mixture (*PCDHA+PCDHG*) and analyzed using ImageJ with the Neuron J plugin (n=60 neurons). Center and error bars show mean ± SEM. The asterisk indicates $p < 0.05$ compared to the negative control.

See also Supplementary Fig. 10. For detailed statistics information, see Supplementary Table 17–18.

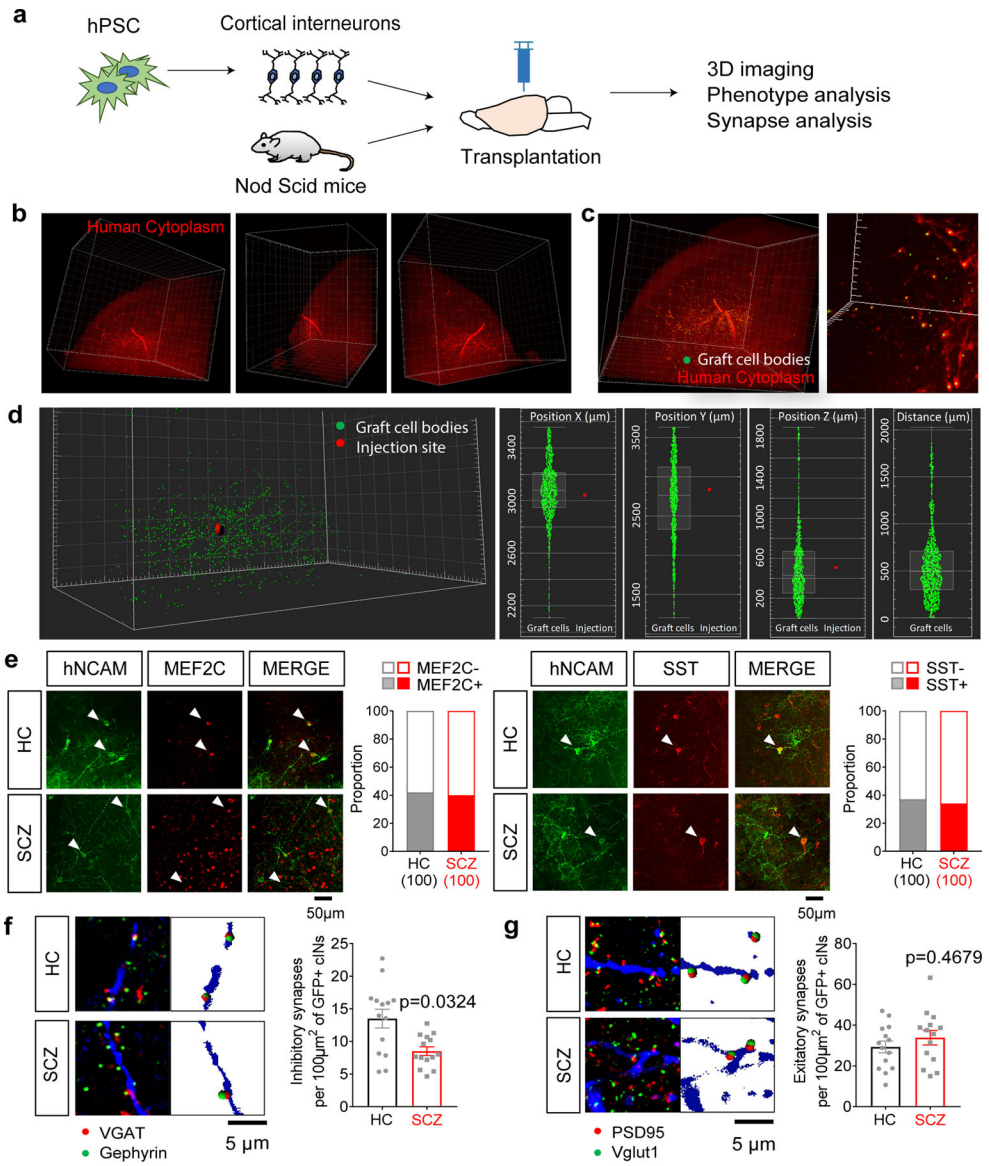

Figure 7. Developing SCZ cINs show synaptic deficit *in vivo* after transplantation into mice brains.

The lines used in each experiment are summarized in Supplementary Table 3. The breakdown data for each line are summarized in Supplementary Table 12.

(a) Schematic diagram of transplantation analysis of HC vs. SCZ cINs.

(b) 3D Lightsheet microscopy images of an iDISCO+-cleared mouse cortex transplanted with iPSC-derived human cINs, stained with human cytoplasm antibody. Major grid in reference frame is 300 μm. This result is from a single whole brain staining.

(c-d) Recognition of grafted neurons by Imaris software shown by green dots. Note that the cells in the front look bigger with bigger green dots and the cells in the back look smaller with smaller green dots. Graphs depict the location of grafted cells along the X, Y, Z axes and distance from the injection site. This result is from a single whole brain staining.

(e) Immunocytochemistry analysis of transplanted cINs 7 months after grafting (scale bar = 50 μm). *Left*: MEF2C^{+} neurons among human NCAM^{+} grafted neurons (p = 0.7737, chi-

square test). *Right*: SST^+ neurons among human $NCAM^+$ grafted neurons (p = 0.6575, chi-square test). White arrowheads indicate double-positive neurons.

(f) Inhibitory synapse analysis on transplanted GFP^+ cINs 4 months after grafting. The data are presented as the number of inhibitory synapses (juxtaposed GFP^+VGAT^+ puncta and $Gephyrin^+$ puncta) per 100 μm^2 of GFP^+ cINs. Center and error bars show mean ± SEM (n = 14 116 μm × 116 μm images per group).

(g) Excitatory synapse analysis on transplanted GFP^+ cINs 4 months after grafting. The data are presented as the number of excitatory synapses (juxtaposed GFP^+PSD95^+ puncta and $Vglut1^+$ puncta) per 100 μm^2 of GFP^+ cINs. Center and error bars show mean ± SEM (n = 14 116 μm × 116 μm images per group).

See also Supplementary Fig. 11. For detailed statistics information, see Supplementary Table 17.

a

HC						SCZ					
Cohort	ID	Gender	Age	PMI	Brain region	Cohort	ID	Gender	Age	PMI	Brain region
McLean	6325	Male	66	22.1	PFC	McLean	10308	Female	62	23.16	PFC
	10477	Male	46	28.83	PFC		10963	Male	46	29.06	PFC
	16799	Male	43	14.68	PFC		853	Male	43	18.16	PFC
	10040	Male	48	24.32	PFC		12413	Male	48	21.83	PFC
	8536	Female	46	17.95	PFC		3019	Female	47	31.85	PFC
Univ. of Maryland	4228	Female	44	16	PFC	HBSFRC	2464	Female	44	15	PFC
	5723	Male	28	28	PFC		1545	Male	28	27.5	PFC
Univ. of Pittsburg	13237	Male	25	22.3	PFC	Univ. of Pittsburg	13097	Male	25	24.3	PFC

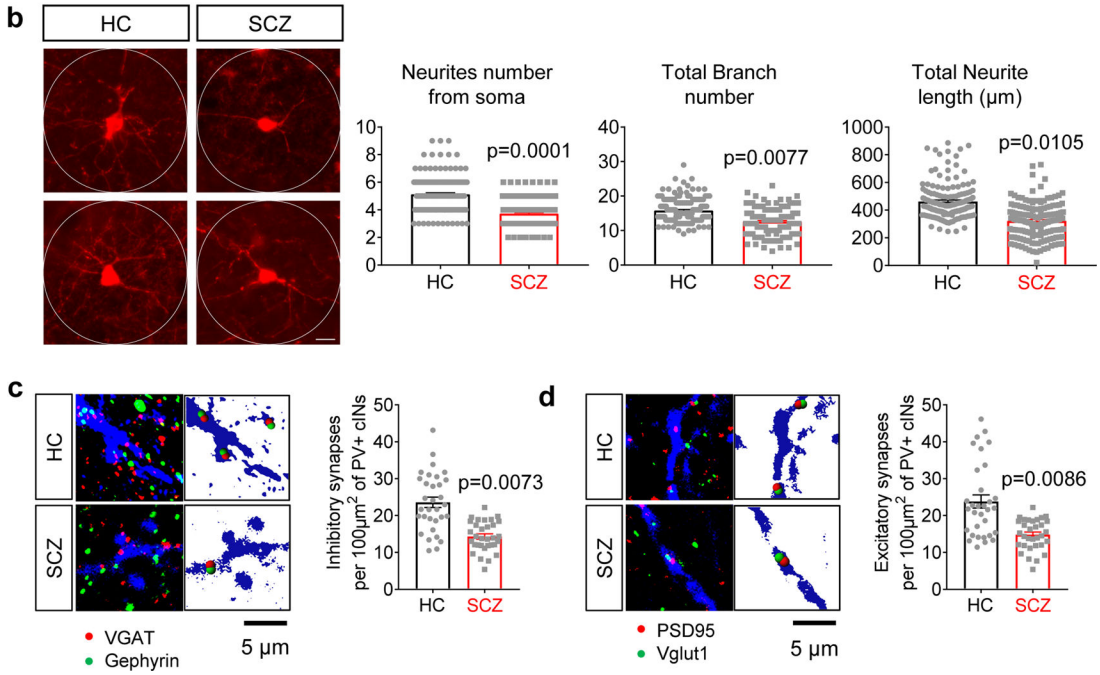

Figure 8. SCZ cINs in postmortem tissue show similar deficit as in developmental SCZ cINs.

The breakdown data for each line are summarized in Supplementary Table 13–14.

(a) Table of subjects used in the postmortem study.

(b) Arborization analysis of layer 3 PV^+ cINs in HC and SCZ postmortem PFC. Arborization within 150 μm of the cell body was traced and analyzed using ImageJ with the Neuron J plugin. Data are presented as mean ±SEM (n = 160 neurons).

(c-d) Synapses analysis of layer 3 PV^+ cINs in HC and SCZ postmortem PFC using Imaris software. For inhibitory synapse analysis on PV^+ cINs, the data are presented as the number of inhibitory synapses (juxtaposed PV^+VGAT^+ puncta and $Gephyrin^+$ puncta) per 100 μm^2 of PV^+ cINs. For excitatory synapse analysis on PV^+ cINs, the data are presented as the number of excitatory synapses (juxtaposed PV^+PSD95^+ puncta and $Vglut1^+$ puncta) per 100 μm^2 of PV^+ cINs. Data are presented as mean ±SEM (n = 32 116 μm × 116 μm images). See also Supplementary Fig. 12. For detailed statistics information, see Supplementary Table 17.